RPN 93

UNCLASSIFIED

DASA 2315

DATE: June, 1968

STUDY AND DEVELOPMENT OF HIGH INTENSITY STOPPED BEAM PLASMA SOURCES (U)

FINAL REPORT

"This work was supported by the Defense
Atomic Support Agency under NWER
subtask LA 013".

HEADQUARTERS
Defense Atomic Support Agency
Washington, D.C. 20305

Ion Physics Corporation
Burlington, Massachusetts

Contract DA-49-146-XZ-553 (II)

ABSTRACT

This report describes studies performed under DASA Contract DA-49-146-XZ-553(II) on the characteristics of the beam-plasma system generated by self-focused electron beams. The effects of the plasma characteristics and drift chamber geometry on propagation are discussed. Studies of the characteristic (line) X-rays are described as well as ultra-violet and visible region observations of the optical emission spectra in H_2, He, O_2 and Ar under typical beam entrance conditions of 40 kA at a mean energy of 1. 5 MeV. The acceleration of light ions by the beam plasma system is demonstrated. Calculations are presented concerning the effect of the return current and the driving azimuthal magnetic field late in the pulse.

FOREWORD

During the period of this contract, April through December 1968, studies were conducted covering beam propagation, plasma radiation and ion motion. The background for these studies is documented in References 1 and 2.

The contributors to these studies were:

S. Graybill	Project Manager and Experimental Studies of Beam Motion and Ion Production
G. Ames	Electrical Diagnostics, Experimental Investigations
J. Rizzo	Optical Diagnostics
J. Uglum W. McNeill	Analysis and Computation
F.K. Childers	Beam Transport Investigations
S.V. Nablo	IPC Director of Research

We would like to acknowledge the cooperation of W. R. Van Antwerp of USANDL in the continued use of his spectrometer apparatus. The assistance of A. Guenther of AFWL and W. Lupton of NRL in the loan and use of diagnostic equipment has been appreciated.

TABLE OF CONTENTS

Section			Page
1	BEAM PROPAGATION		1
	1.1	Introduction	1
	1.2	Plasma Space Charge and Current Effects	1
	1.3	Beam Propagation Velocity	8
	1.4	Image Current Guiding of the Beam	18
2	CHARACTERISTIC X-RAY RADIATION		22
3	ION ACCELERATION		29
	3.1	Introduction	29
	3.2	D(d, n) Neutrons	29
	3.3	Be(x, n) Neutrons	32
	3.4	Time of Flight Measurements	32
	3.5	Analysis of Longitudinal Ion Acceleration Studies	35
	3.6	Acceleration Region Determination	50
4	OPTICAL AND SPECTROGRAPHIC DIAGNOSTICS		53
	4.1	Review	53
	4.2	Introduction	53
	4.3	Optical Cavity Studies	54
	4.4	Highly Ionized Line Signatures	56
	4.5	Hydrogenic Lines	61
	4.6	Spectral Line Shapes	65
	4.7	Summary	69

TABLE OF CONTENTS (Continued)

Section | Page

5 THEORETICAL INVESTIGATIONS 70

5.1 Return Current in the Hydrodynamic Model 70

5.2 Numerical Results 76

5.3 Azimuthal Magnetic Field in the Wake of the Current Pulse 79

6 REFERENCES 86

LIST OF ILLUSTRATIONS

Figure		Page
1	FX-1 Electron Beam Energy Spectrum	2
2	FX-1 Electron Beam Energy Spectrum	3
3	FX-1 Field Emission Cathode Current Profiles	4
4	Drift Tube and Field Emission Tube Current Shunts	5
5	Drift Tube Current vs Pressure	6
6	Wall Current as a Function of Drift Tube Pressure (Air)	7
7	Rogowski Coil Measurement of Net Current as a Function of Drift Tube Pressure	9
8	Beam Plasma Photographs for a Multi-Point, Low Impedance Cathode	10
9	Beam Plasma Photographs for a Single Point, Low Impedance Cathode	11
10	Beam Plasma Due to Multi-Pin Cathodes and Apertured Anode Geometries	12
11	Stopping Beam - Bremsstrahlung Target	13
12	Electron Beam Front Time of Flight Measurements (100 Ohm Case, Drift Tube Pressure 0.2 torr)	15
13	Electron Beam Front Time of Flight Measurements (30 Ohm Case, Drift Tube Pressure 0.2 torr)	16
14	Pulsed Electron Beam Propagation	17
15	300 cm Propagation of 30 Ohm Beam	19
16	Bending Beam Experiment	20
17	FX-25 Bending Beam Experiment - Deposition Profile	21
18	Beam Plasma Radiation Diagnostics	23
19	Calculated Efficiency of 75 μ Depleted Si Diode with 0.0005 Inch Be Window	24
20	X-Ray Absorption Studies in Be and Al	25
21	X-Ray Yield as a Function of Argon Pressure	26
22	K Edge Absorption Results	28
23	Production Rate of D-D Neutrons From Beam Plasma ($I/\beta\gamma$ = 10,000)	30

LIST OF ILLUSTRATIONS (Continued)

Figure		Page
24	Neutron Anisotropy - 21 Needle Cathode, P-M Tube - Scintillator Detector	31
25	Experimental Arrangement for Beam Plasma Ion Detection	33
26	Representative Ion Pulses	34
27	Representative Proton Flight Time Data	36
28	Time-of-Flight Data for Hydrogen Ions	37
29	Time-of-Flight Data for Deuterium Ions	38
30	Time-of-Flight Data for Helium Ions	39
31	Time-of-Flight Data for Nitrogen Ions	40
32	Dependence of Hydrogen Ion Energy on Primary Beam Current	43
33	Dependence of Hydrogen Ion Arrival Time on Ambient Pressure	44
34	Total Neutron Yields for the Reactions Be(x, n) and D(d, n) as a Function of Filling Pressure	47
35	Summary of Energetic Ion Data	48
36	Typical Radial Ion Detection System	49
37	Measurement of Ion Acceleration Length 20 Pin Cathode, 30 Ohm Gap	51
38	Radial Collimation of D(d, n) Neutrons	52
39	Electron Beam Pumped Optical Cavity	55
40	Electron Beam Produced Plasma Stimulated Emission	57
41	Vacuum UV Experimental Setup	59
42	Self-Stopped Electron Beam Produced Plasmas (Typical Oxygen Signatures)	60
43	Axial He II 3203 Å Line Signatures for Three Drift Tube Lengths	63

LIST OF ILLUSTRATIONS (Continued)

Figure Page

44 Oxygen Plasma Spectra (Axial View) Produced by Propagating $\nu_o/\gamma > 1/2$ Electron Beam Wavelength Region 4328 Å to 4366 Å 66

45 Oxygen Plasma Spectra (Axial View) Produced by Propagating $\nu_o/\gamma > 1/2$ Electron Beam Wavelength Region 2878 Å to 2930 Å 67

46 Oxygen Plasma Spectra (Normal View) Produced by Propagating $\nu_o/\gamma > 1/2$ Electron Beam Wavelength Region 4328 Å to 4366 Å 68

47 Return Current Density at Various Radii $\sigma = 2$ mho/cm 74

48 Return Current Density at Various Radii $\sigma = 20$ mho/cm 77

49 Return Current Density at Various Radii $\sigma = 2.0 \times 10^4$ mho/cm 78

50 Model for Wake Calculation 80

51 Wake Magnetic Field Intensity 84

SECTION 1

BEAM PROPAGATION

1.1 Introduction

The beam propagation experiments conducted over the past year have utilized several beams reproducible enough to be considered standard. One is the 100 ohm beam produced by the 1/8 inch diameter cathode, the energy spectrum of which is shown in Figure 1. A second which has been used extensively since the early observations of beam stopping at currents near the Lawson limit is the 30 ohm beam produced by a 20 pin array of emitters. Its spectrum is shown in Figure 2. The current pulses of both of these beams are shown in Figure 3.

1.2 Plasma Space Charge and Current Effects

The roles of space charge neutralization and plasma current magnetic neutralization were discussed in great detail in Reference 1. In that report the results of calorimetry and current measurements on the 100 ohm beam with a Rogowski loop were cited. Experiments conducted during this phase of study with the 30 ohm beam using the drift tube wall return current monitor, have confirmed those earlier findings. The current shunt configuration is shown in Figure 4. In Figure 5 the return current data monitored in a 15 cm diameter drift tube at z = 50 cm are shown with the reduced data in Figure 6. One sees the expected focusing effect resulting from space charge neutralization which maximizes at a pressure of 0.2 torr and the countering effect of plasma return currents which neutralize the magnetic focusing from 2 torr to 10 torr. Above 10 torr the plasma conductivity decreases due to collisions, forcing the return current to flow in the wall and the beam again focuses. These results are in agreement with previous findings. However, these data (Figure 5) also show the long, ≈0.5 μs, inductively driven current which follows the beam. This was not shown in the Rogowski coil data reported earlier(1) due to the 200 ns L/R slump of the coil. Comparable

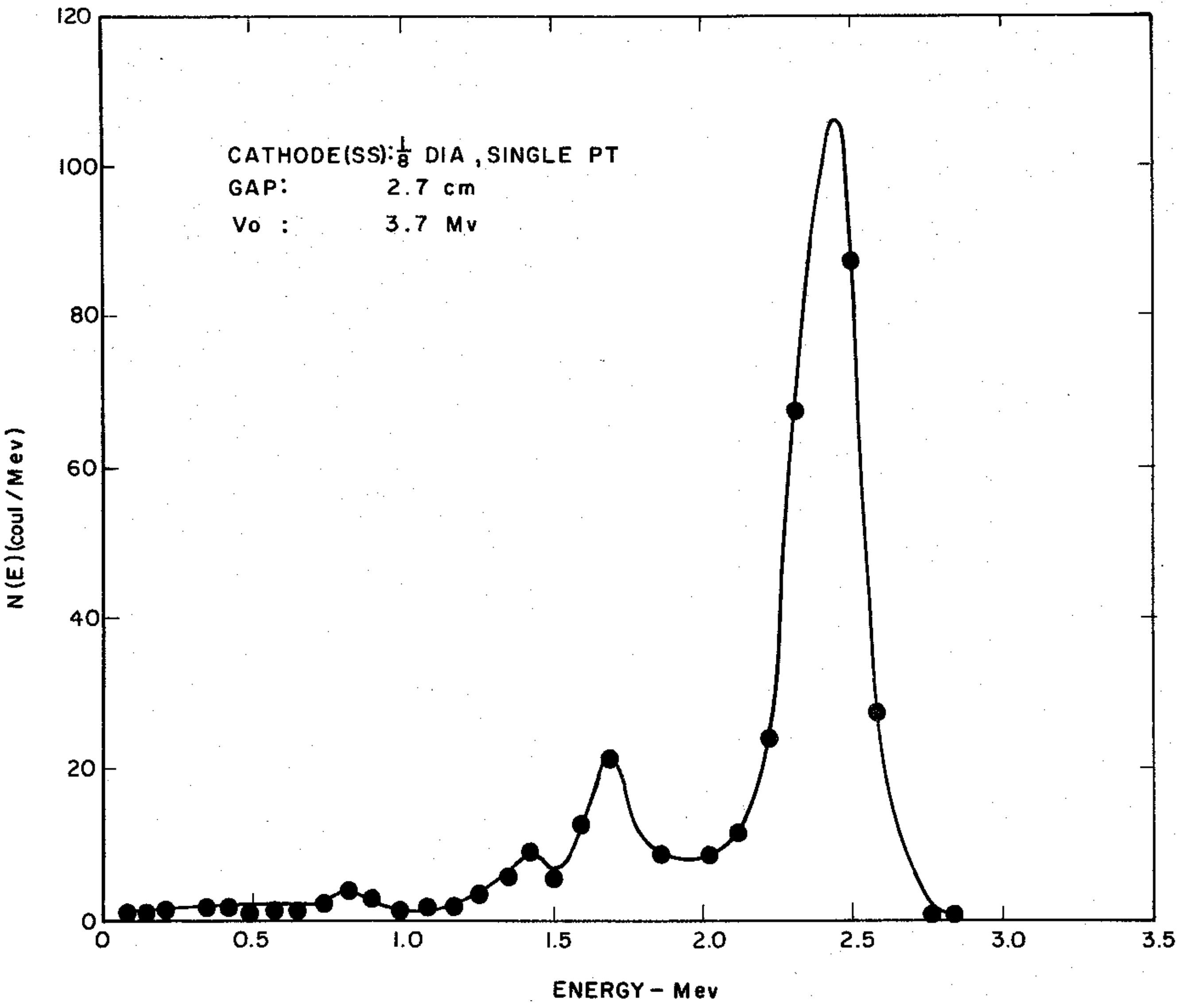

Figure 1. FX-1 Electron Beam Energy Spectrum

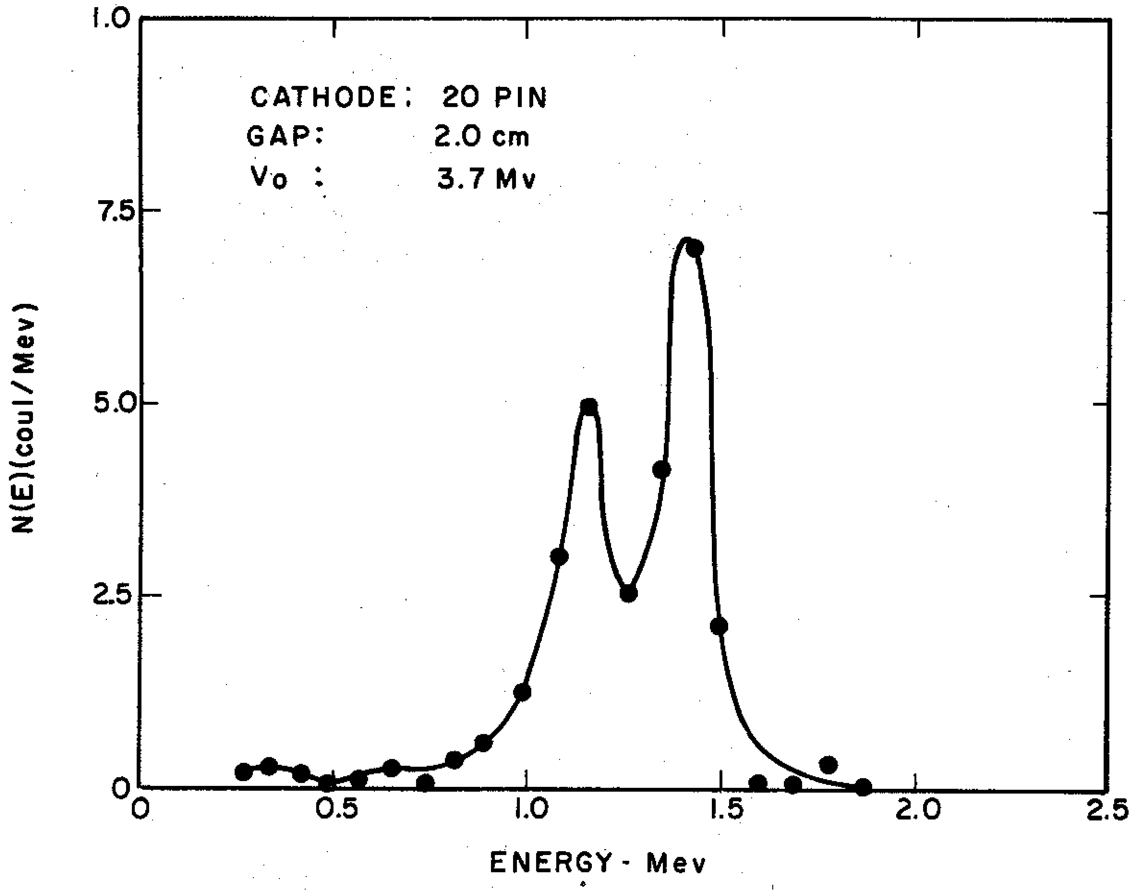

Figure 2. FX-1 Electron Beam Energy Spectrum

1-2597

Single Point Cathode

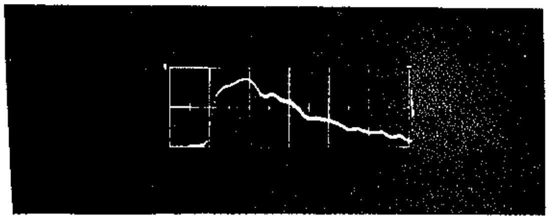

Horizontal Scale: 20 nsec/div
Vertical Scale: 13,000 A/div
I_{max} = 22,000 A

20 Point Cathode

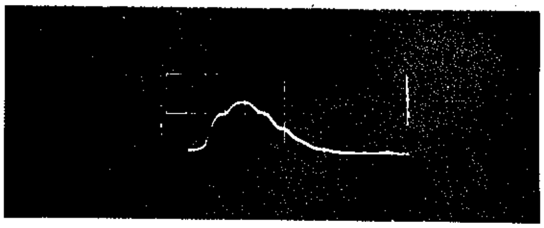

Horizontal Scale: 20 nsec/div
Vertical Scale: 32,000 A/div
I_{max} = 39,000 A

Figure 3 FX-1 Field Emission Cathode Current Profiles

2-824

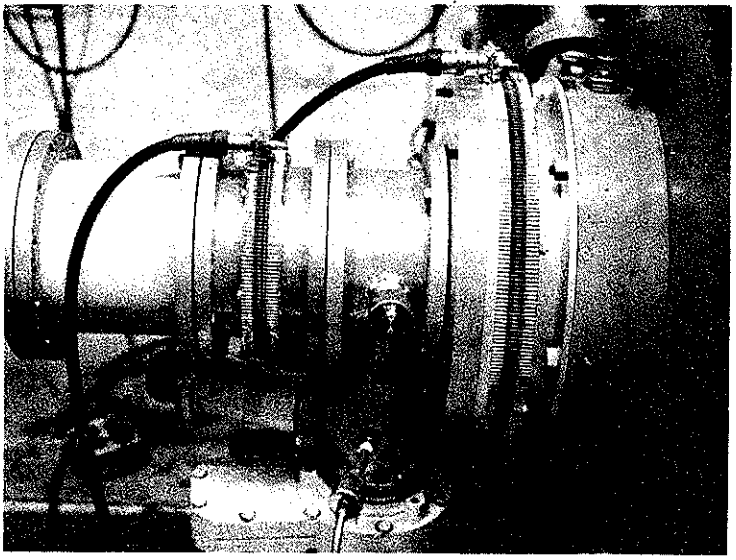

Figure 4. Drift Tube and Field Emission Tube Current Shunts

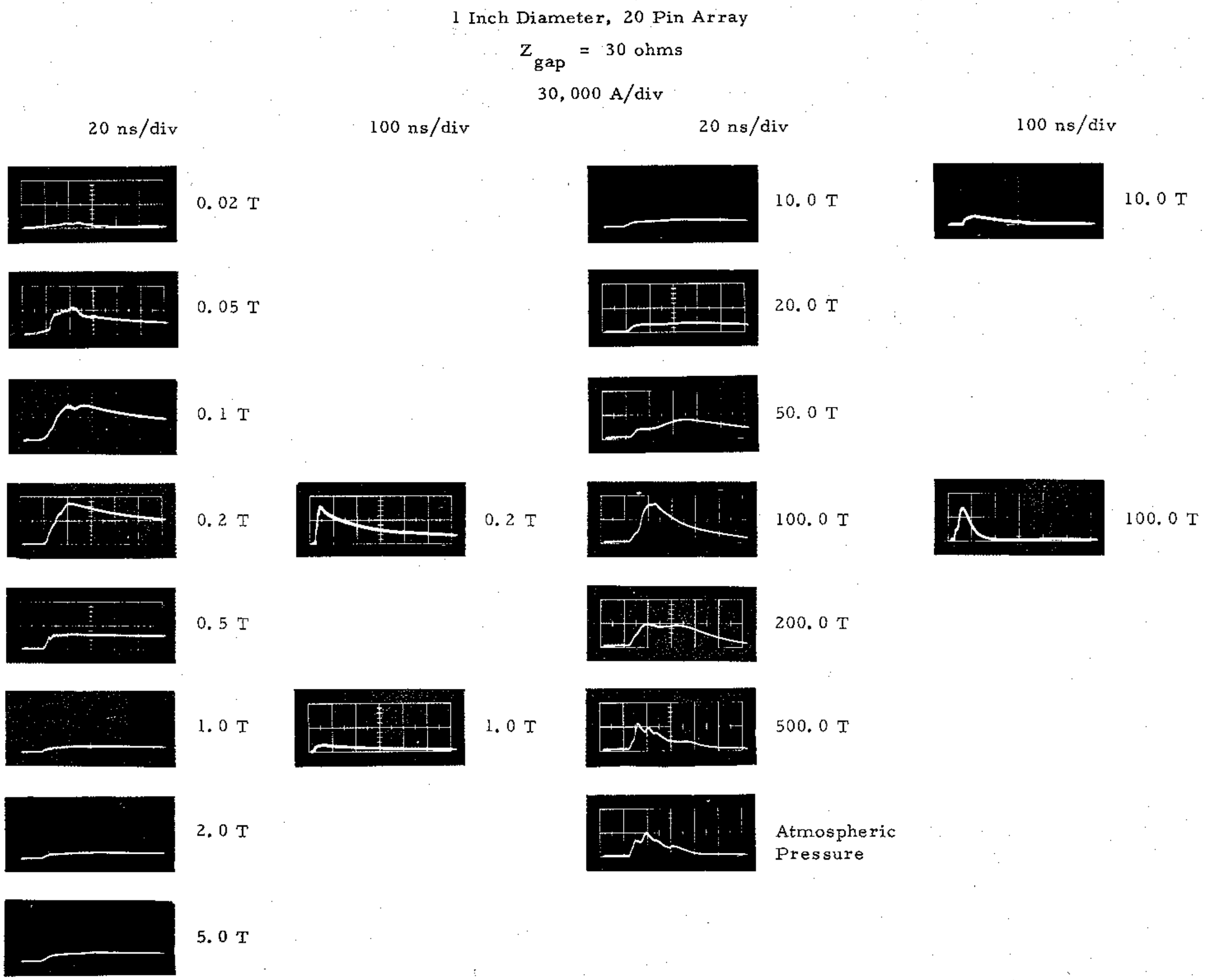

Figure 5. Drift Tube Current vs Pressure

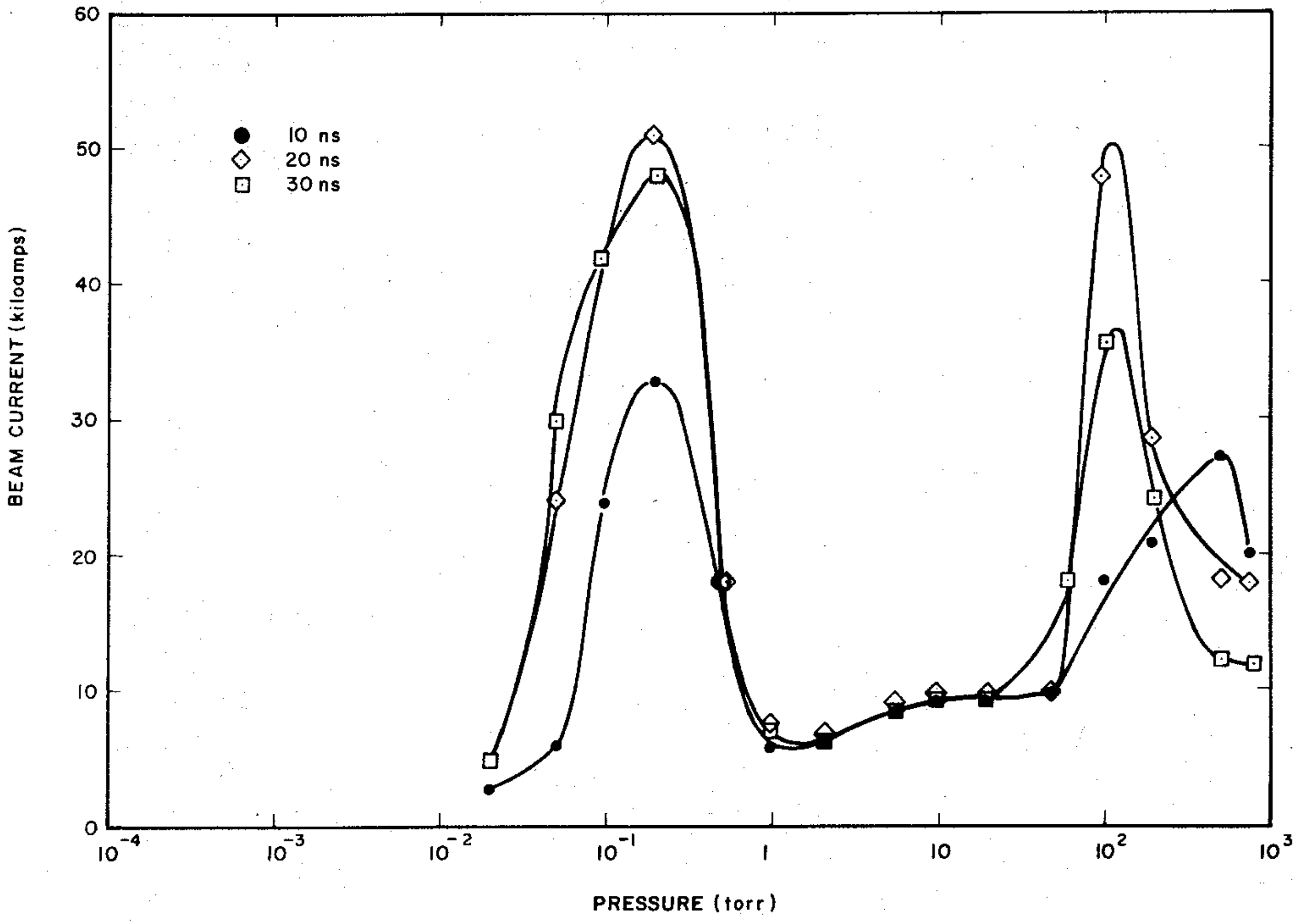

Figure 6. Wall Current as a Function of Drift Tube Pressure (Air)

Rogowski data for the same pressure range are shown in Figure 7, taken at the z = 20 cm location with the 100 ohm beam.

Open shutter photography studies were made of the 30 ohm beams from the 1-inch diameter 20 pin cathode, the single point cathode with a short gap (0.7 cm) and gassy (5×10^{-3} torr) tube, and the single point cathode under the same short gap and gassy tube condition with an apertured carbon anode. The aperture was varied from 0.5 to 1 cm. All three of these conditions delivered 40,000 A at 1 to 1.5 MeV. This produces a ν/γ of 0.7.

Figures 8 and 9 show the beams from the 20 pin cathode and the single point high current configuration at three pressures. At 0.2 torr and 100 torr the beams are pinched and, in the case of the single point injector, they stop. Both beams propagate in the force free regime of 1.0 torr. These confirm the roles of charge neutralization and return current and demonstrate that beam stopping is dependent on the injection geometry. That is, the high current density injection condition is more conducive to beam stopping. This is confirmed by use of the beam from the apertured anode as shown in Figure 10. The drift region is held at 0.2 torr and the field emission tube at 5×10^{-3} torr with differential pumping. The gap is 0.5 cm.

Figure 11 shows confirming evidence of the stopping of the beam at high and low gas pressures and the propagation at 1 torr. The technique used here employs a tantalum bremsstrahlung target which can be positioned at predetermined longitudinal (z) positions in the drift tube. The radiation signature generated from it, as observed with an external fast photodiode-scintillator, is used to infer the primary stream characteristics. It was demonstrated in a separate experiment that the bremsstrahlung observed at 0.2 and 100 torr is mostly from the window.

1.3 Beam Propagation Velocity

Early investigations of beam propagation performed in 1965 to evaluate these self-focused streams for fast reactor applications inducated that

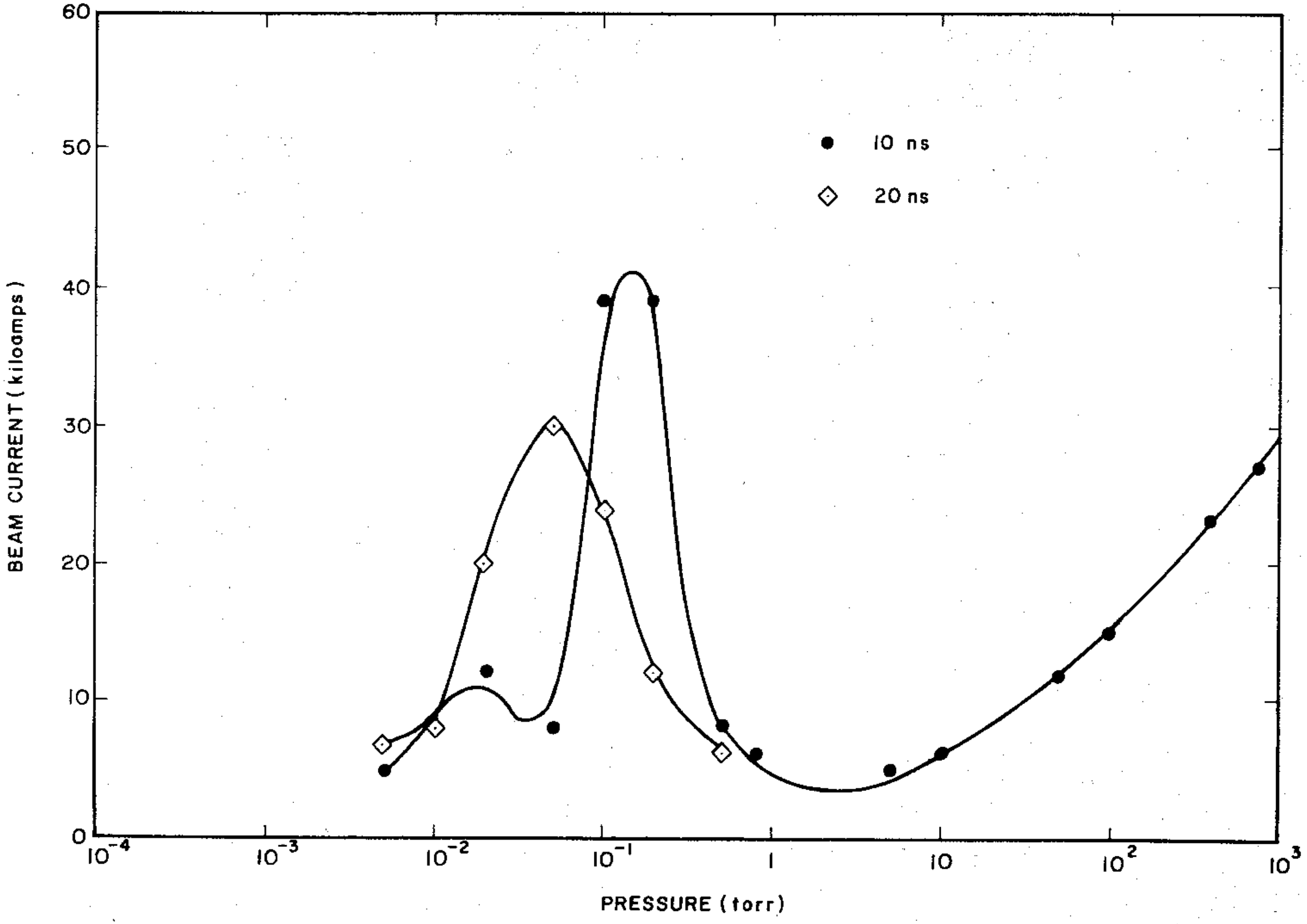

Figure 7. Rogowski Coil Measurement of Net Current as a Function of Drift Tube Pressure

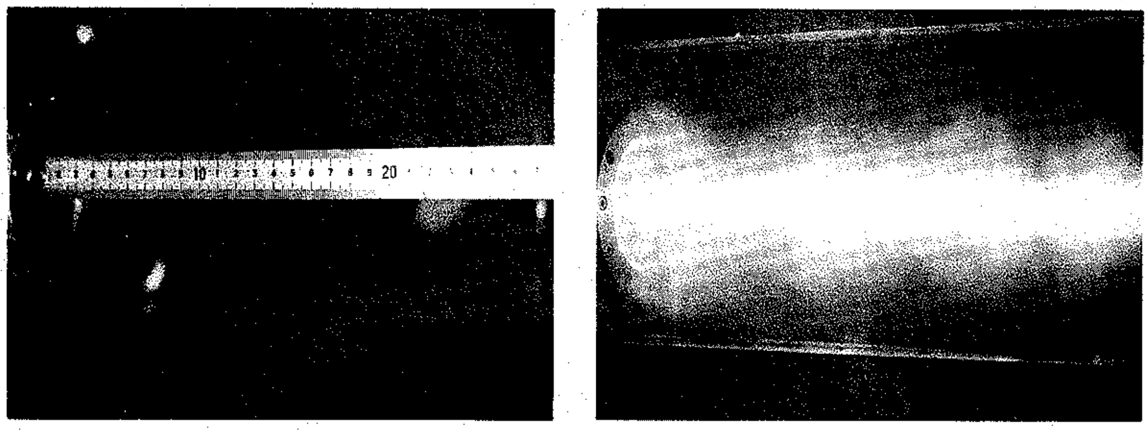

(a) Calibration Scale

(b) Ambient Pressure = 0.2 torr (Air)

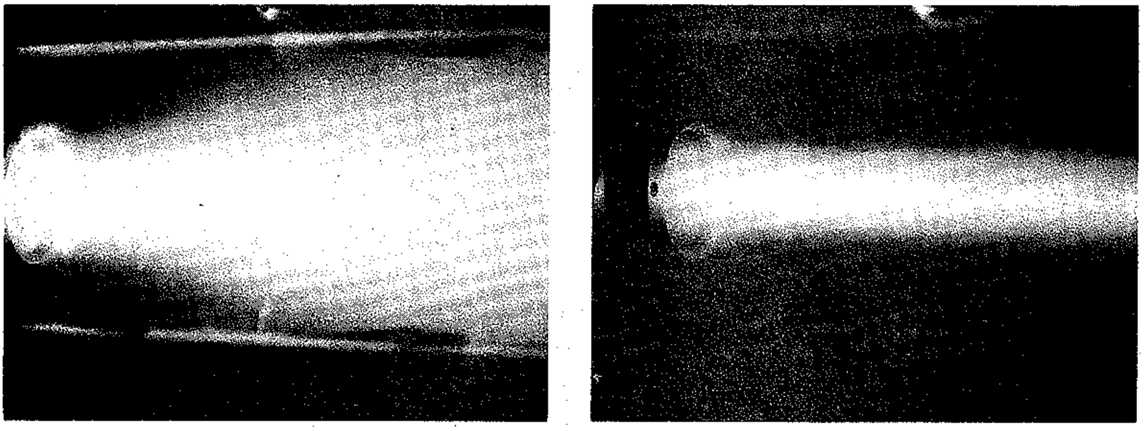

(c) Ambient Pressure = 1.0 torr (Air)

(d) Ambient Pressure = 100.0 torr (Air)

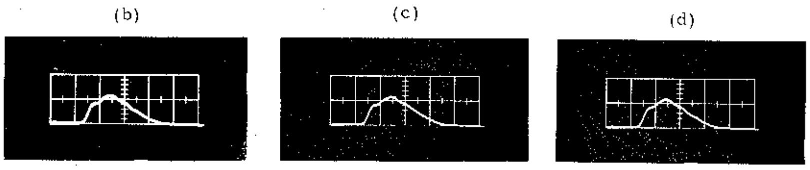

Beam Current Profile
Vertical Scale = 33.0 kA/cm
Horizontal Scale = 20.0 ns/cm

Figure 8 Beam Plasma Photographs for a Multi-Point, Low Impedance Cathode

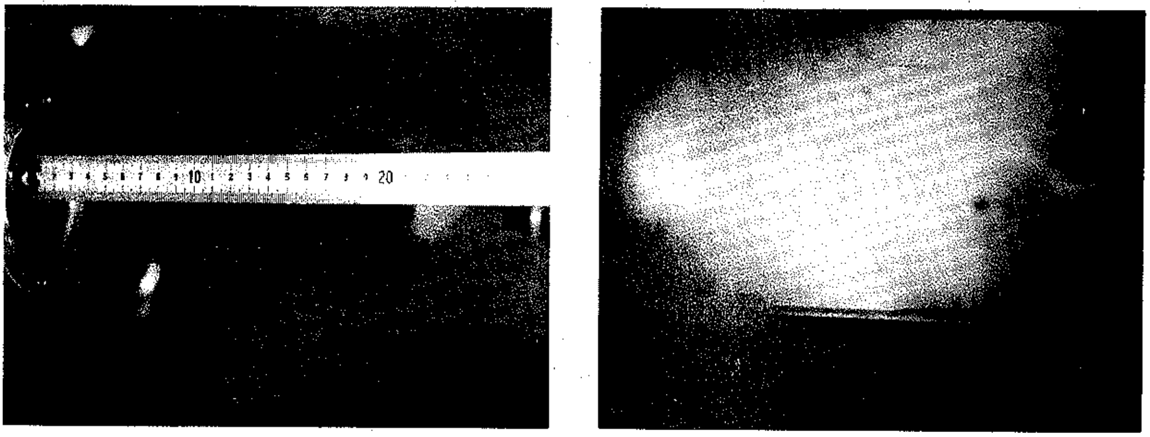

(a) Calibration Scale

(b) Ambient Pressure = 0.2 torr (Air)

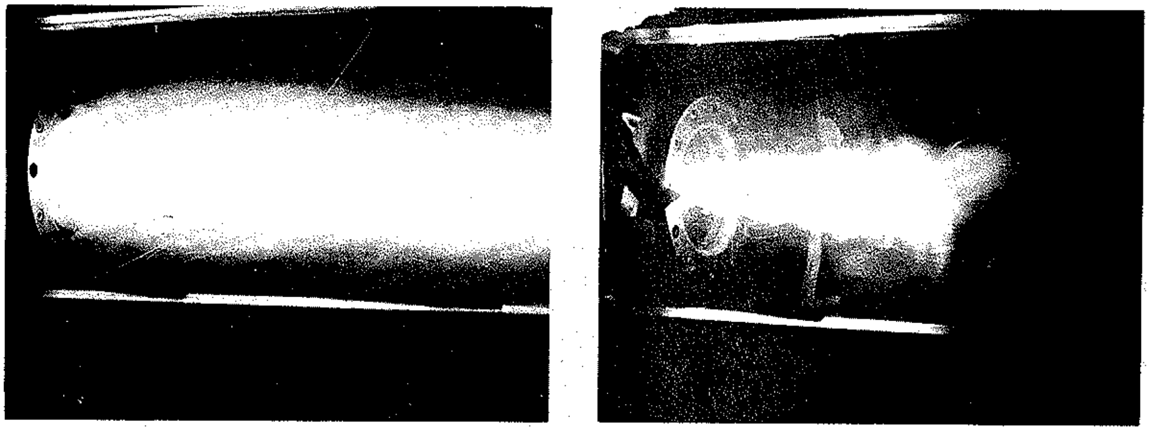

(c) Ambient Pressure = 1.0 torr (Air)

(d) Ambient Pressure = 100.0 torr (Air)

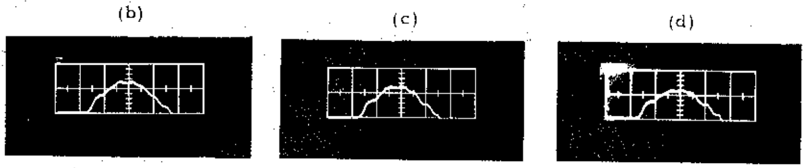

Beam Current Profile
Vertical Scale = 33.0 kA/cm
Horizontal Scale = 20.0 ns/cm

Figure 9 Beam Plasma Photographs for a Single Point, Low Impedance Cathode

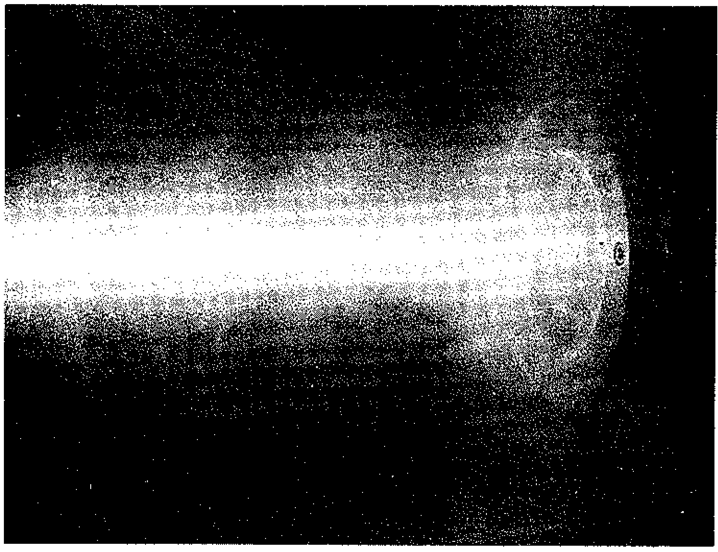

20 Pin Array, 2 cm Gap, $P_o = 0.2$ T, $P_T = 10^{-4}$ T,
I = 40,000 amp, $V_{beam} = 1$ to 1.5 Mev

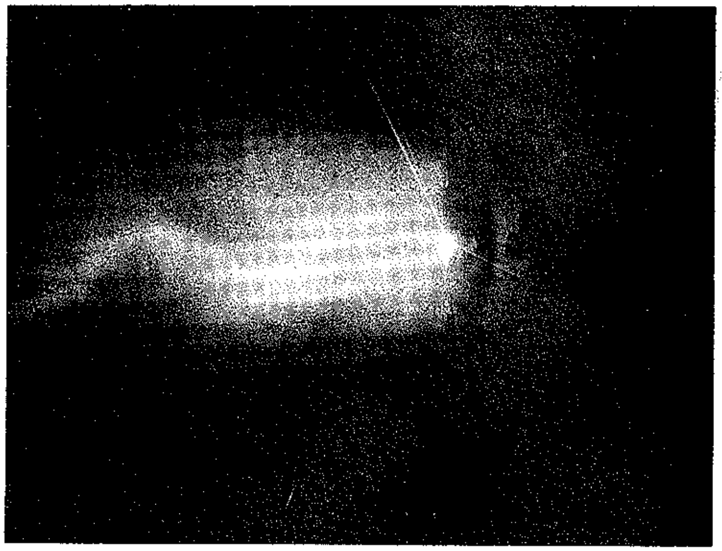

0.5 cm Aperture, 0.5 cm Gap, $P_o = 0.2$ T, $P_T = 5 \times 10^{-3}$ T,
I = 35,000 amp, $V_{beam} = 1$ Mev

Figure 10 Beam Plasma Due to Multi-Pin Cathodes and Apertured Anode Geometries

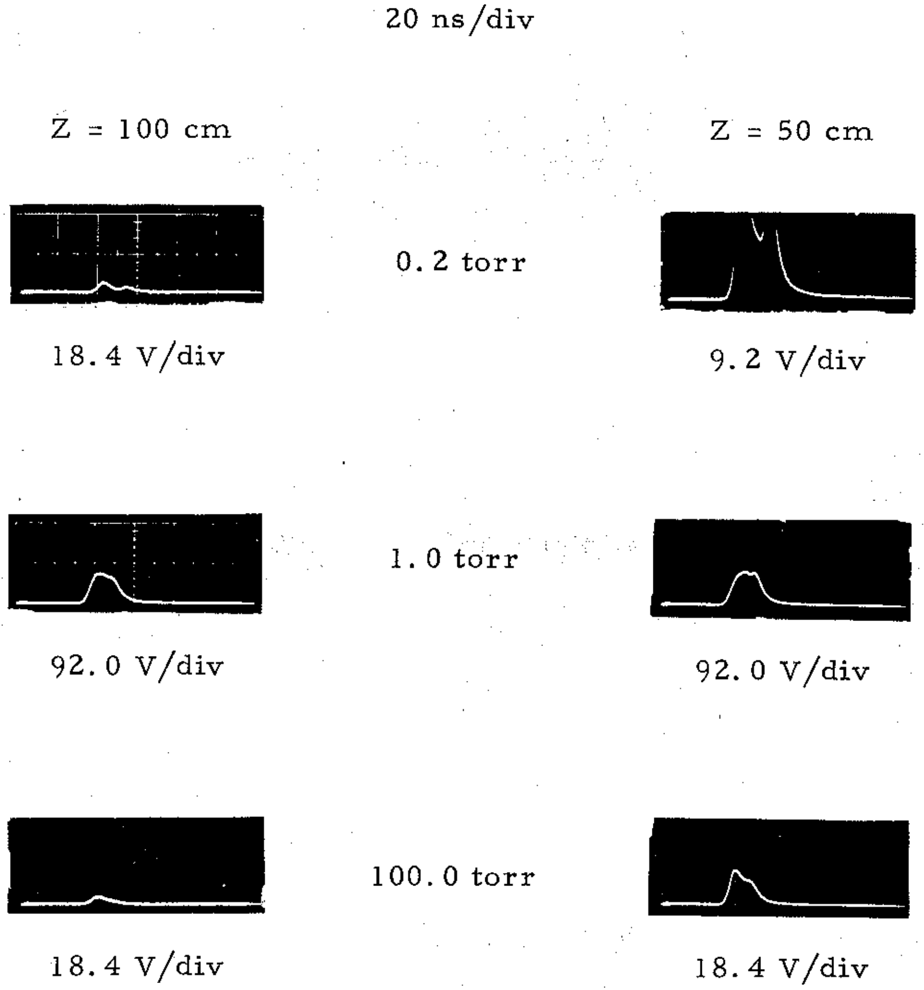

Figure 11 Stopping Beam - Bremsstrahlung Target

2-1098

efficient energy transport could be accomplished with e-folding distances of several meters. Under the present program the 100 ohm beam from the single point cathode and the 30 ohm beam produced by the 20 pin cathode were studied with drift lengths of up to 3 m. The diagnostic tools for this study were the return current shunts and the scintillator bremsstrahlung detector used in conjunction with a tantalum target. The results presented here are all referred in time to the initial current pulse.

Figures 12 and 13 show the current and bremsstrahlung signatures at entrance and after 3 m of drift of the 100 ohm beam and of the 30 ohm beam. We see that drift tube current starts about 2 ns after the field emission current, probably due to window absorption and scatter of the low energy electrons in the first 2 ns of the pulse. The current detected at 300 cm is 90% of the injection current in the case of the 100 ohm beam and 60% for the 30 ohm beam. The drift tube current signatures display a long decay due to plasma currents driven by the collapsing B field. The bremsstrahlung pulses show that after 300 cm drift distance, the maximum electron energy occurs later, with reference to the beam front, than at the injection plane ($z = 0$ cm). This is probably due to the inductive retardation of the beam front and acceleration of the decaying portion of the current pulse.

The bremsstrahlung signal in both beams shows a small early pulse followed by a larger late pulse. The data indicate that the early pulse is due to window and side wall bremsstrahlung. Figure 14 shows arrival time versus drift distance for the early and late bremsstrahlung pulses and the current front. The arrival times are referred to an arbitrary, but constant reference time. It is seen that the early pulse demonstrated a β of unity as it should if the source of this bremsstrahlung is fixed. An observed decrease of amplitude of this signal, as the detector was moved downstream with the bremsstrahlung target, also indicated that it originated at the window plane.

The plot of the late bremsstrahlung pulse shows that it demonstrates about the same propagation velocity as the beam front, but delayed in time from it by a constant interval of ~ 10 ns. It is significant that this is approximately

1/8 Inch Diameter, Single Point Cathode
$Z_{gap} \approx 100$ Ohms

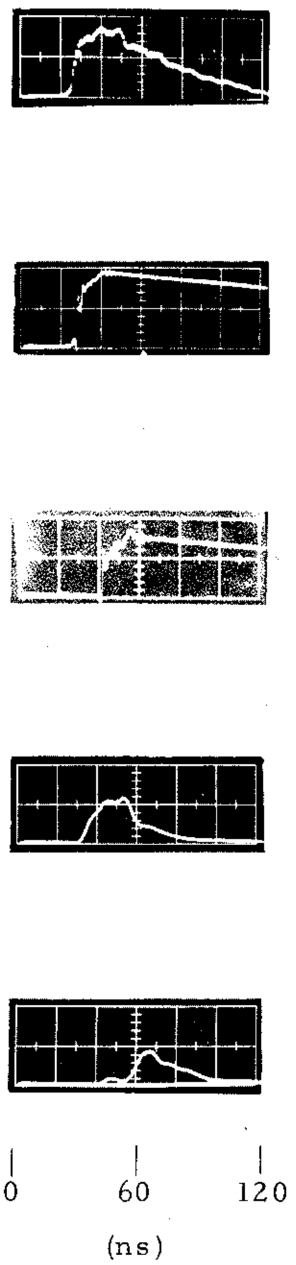

Field Emission Current
13, 000 A/div

Drift Tube Current
Z = 6 cm
11, 500 A/div

Drift Tube Current
Z = 300 cm
11, 500 A/div

Bremsstrahlung Target at Z = 0
Detector at Z = 0, r = 30 cm
92 V/div

Bremsstrahlung Target at Z = 300 cm
Detector at Z = 300 cm, r = 30 cm
92 V/div

Figure 12 Electron Beam Front Time of Flight Measurements (100 Ohm Case, Drift Tube Pressure 0.2 Torr)

2-1078

1 Inch Diameter, 20 Pin Array Cathode
$Z_{gap} = 30$ Ohms

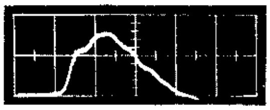

Field Emission Current
33,000 A/div

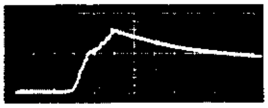

Drift Tube Current
Z = 6 cm
29,000 A/div

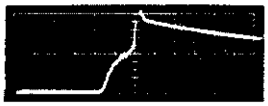

Drift Tube Current
Z = 300 cm
11,500 A/div

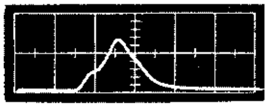

Bremsstrahlung Target at Z = 0
Detector at Z = 0, r = 30 cm
92 V/div

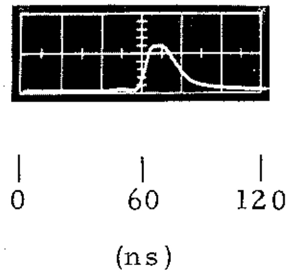

Bremsstrahlung Target at Z = 300 cm
Detector at Z = 300 cm, r = 30 cm
46 V/div

Figure 13 Electron Beam Front Time of Flight Measurements (30 Ohm Case, Drift Tube Pressure 0.2 Torr)

2-1079

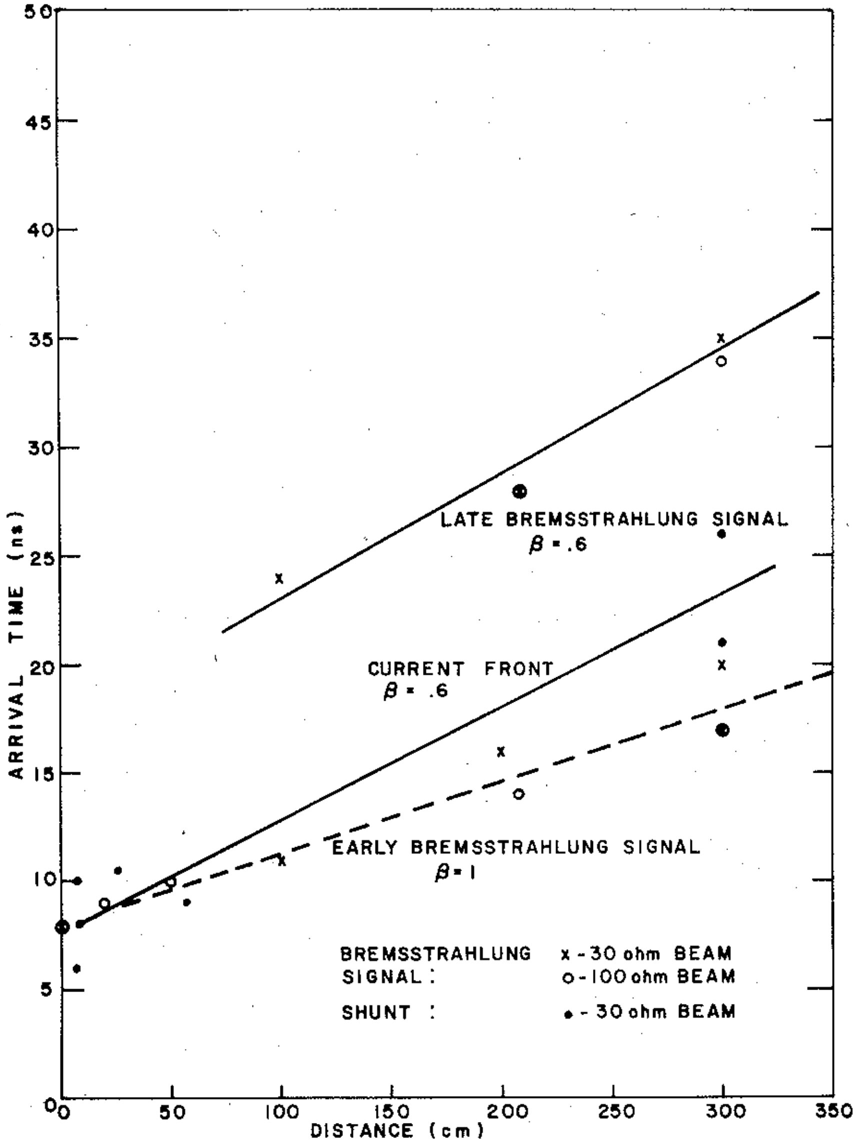

Figure 14. Pulsed Electron Beam Propagation

1-3568

the neutralization time (when f = $1 - \beta^2$) for the injection conditions, suggesting that the energetic electron flow is delayed by the time to neutralize the stream.

Figure 15 shows drift tube current shunt data and bremsstrahlung data for the 30 ohm beam after 300 cm of drift for various pressures. Unlike studies performed with short drifts, these results show very little current at 100 torr at this drift distance. Also, the 0.2 torr current is greater than that at 1.0 torr by a factor of 4 as is seen in short drift experiments, but the bremsstrahlung signal is larger by a factor of 2 at 1 torr, indicating better energy transfer. It is interesting to note that the current which traverses the 300 cm system at 100 torr drift pressure comes very late in time.

1.4 Image Current Guiding of the Beam

The deflection of a beam from a conducting surface has been observed here and at other laboratories. The "guiding" mechanism is the magnetic repulsion due to the return current induced in the conductor. This force provides a stable equilibrium for a beam in a conducting tube. This also suggests using these induced current forces for the purpose of guiding the beam in a curved path.

An experiment using a 3 m flexible conduit for a drift tube was conducted with current measurements made in a straight configuration and with a radius of curvature (3.2 m) such that the beam experienced a 45-degree change in direction. The conditions were not optimized, but these preliminary results are encouraging.

The data presented in Figure 16 shows that we get one-half of the injection current at 300 cm in the straight tube and one-half of that with a 45 degree bend. It is also noted that there is suppression of the early part of the pulse or a longer transit time in the curved configuration. As always, these results are referred in time to the injection pulse.

Figure 17 shows the energy as determined by depth dose measurements and shows no degradation in the curved configuration as opposed to the straight geometry.

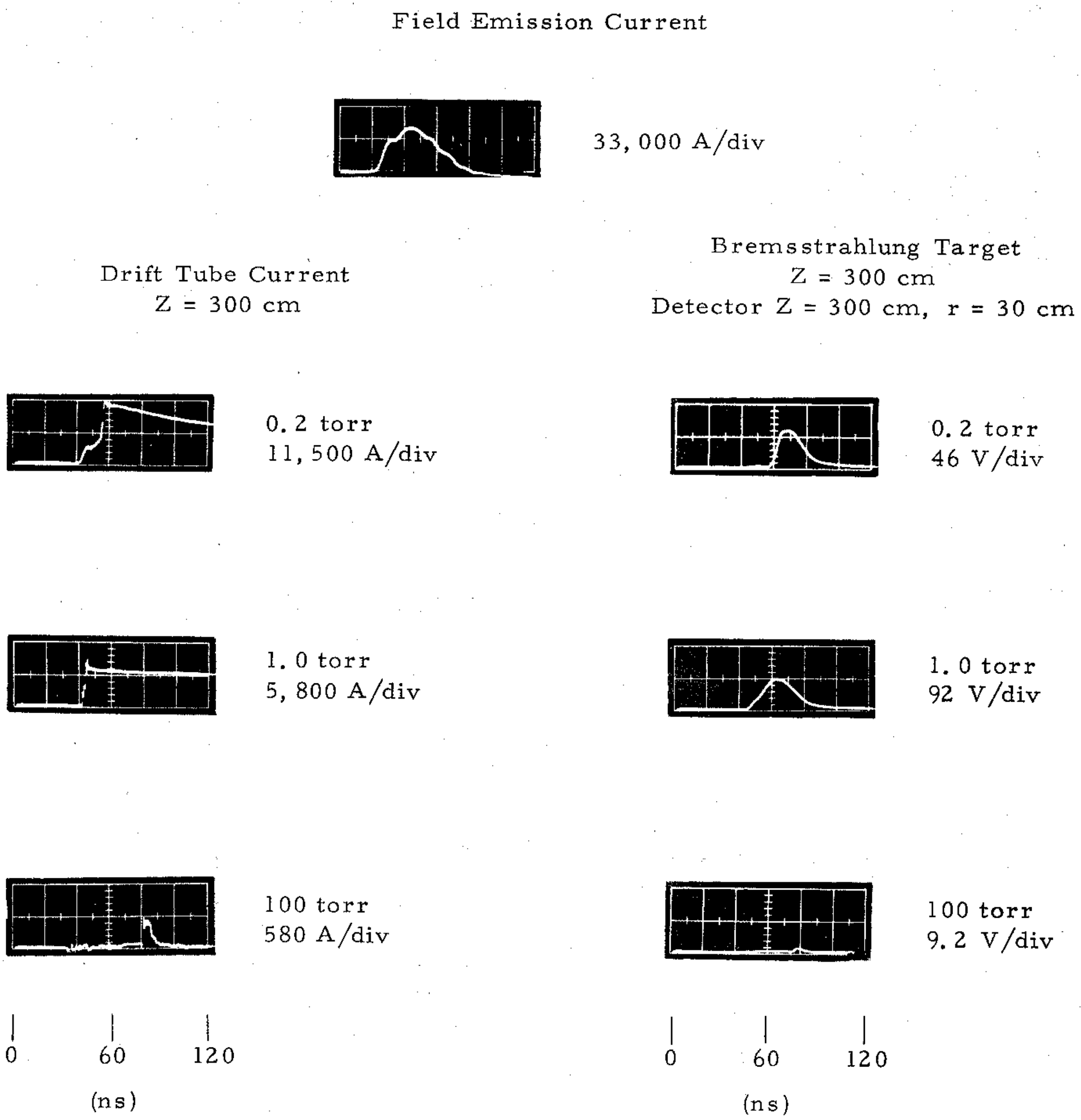

Figure 15 300 cm Propagation of 30 Ohm Beam

2-1080

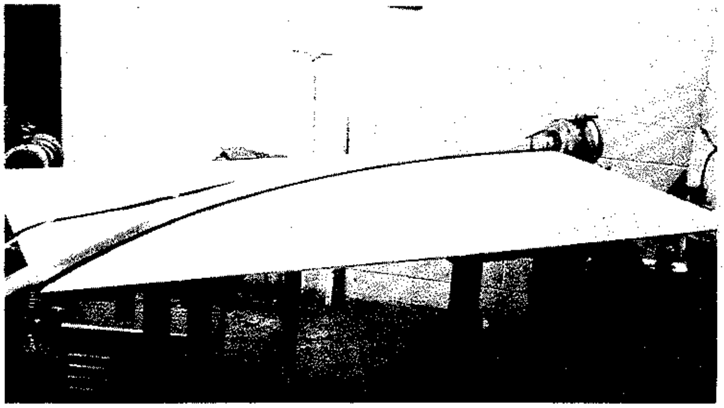

Experimental Arrangement on FX-25 (45 deg Bend)

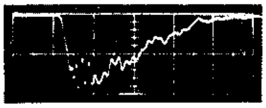

Field Emission Tube Current
20 ns/div
12, 000 A/div

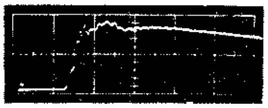

Drift Tube Current
Z = 6 cm
12, 000 A/div
20 ns/div

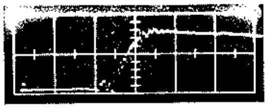

Drift Tube Current
Z = 300 cm
Straight Tube
6500 A/div
20 ns/div

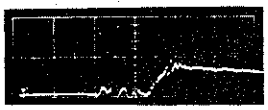

Drift Tube Current
Z = 300 cm
45 deg Bend
6500 A/div
20 ns/div

Figure 16 Bending Beam Experiment

2-1082

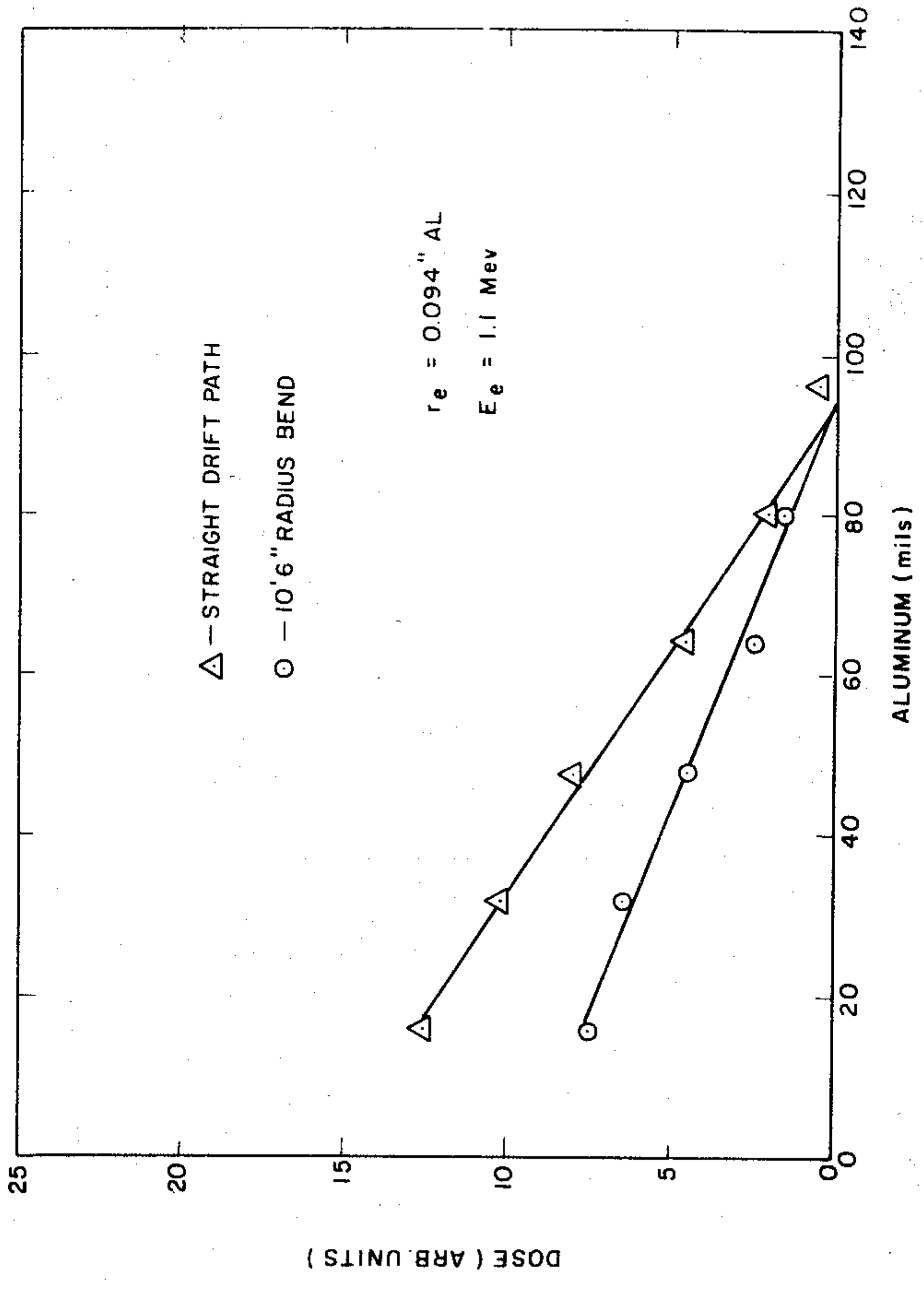

Figure 17. FX-25 Bending Beam Experiment - Deposition Profile

SECTION 2

CHARACTERISTIC X-RAY RADIATION

An experimental apparatus to study the 1 to 10 keV photon energy range was constructed and used successfully. In Reference 1, we noted that scattered electrons were a background problem at high pressure, even with a magnetic field applied. This was solved by magnetically deflecting the electrons in a vacuum ($<10\ \mu$) which is low enough that the scatter mean free path is much greater than the pole dimensions. The arrangement is shown in Figure 18. The magnetic deflection region is separated from the plasma by a 0.0005 inch Be window which also shields the detector from optical emission. The detector is also shielded from direct window bremsstrahlung with lead. There are two identical channels, one for absorber experiments and one for normalization.

The detector is an SSR 100-NPS-200 diffused junction diode. The calculated response of this detector with the 0.0005 inch Be window is shown in Figure 19. The characteristic X-ray yield of argon was measured with this arrangement using 100 torr of argon gas as the target.

Absorber studies were performed with beryllium and aluminum. The results are shown in Figure 20. The aluminum point was very near the window bremsstrahlung level and can only be said to have a μ_{eff} of >300. It is important because it demonstrates that we were not detecting electrons, since in that case the aluminum and beryllium results would have shown the same transmission. The radiation pulse was 50 ns in duration, started promptly with the current and lasted for 20 ns after the current pulse. This was shown later to be the solid state detector's collection time and the characteristic X-ray pulse was probably coincident with the current pulse.

The relative yield of radiation as a function of gas pressure is shown in Figure 21. It is compared with a calculated yield assuming yield proportional to neutral density with the self absorption of radiation taken into account. The characteristic line portion of the radiation would be expected to behave in this manner.

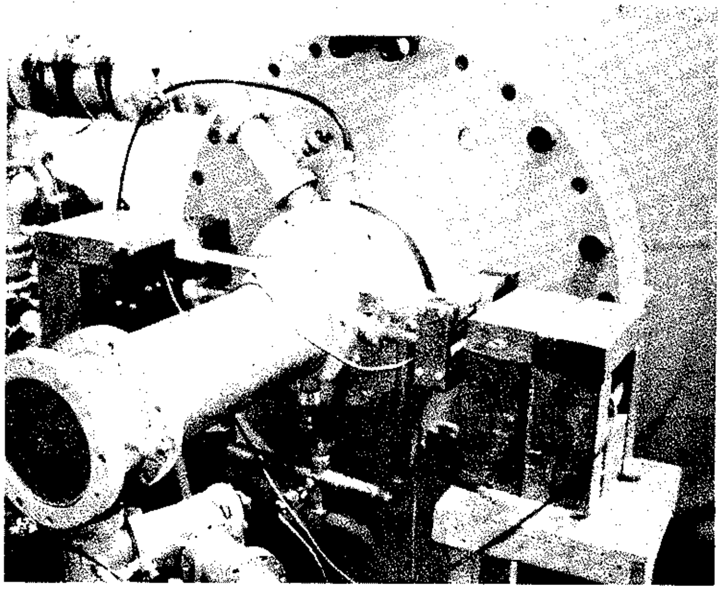

Figure 18 Beam Plasma Radiation Diagnostics

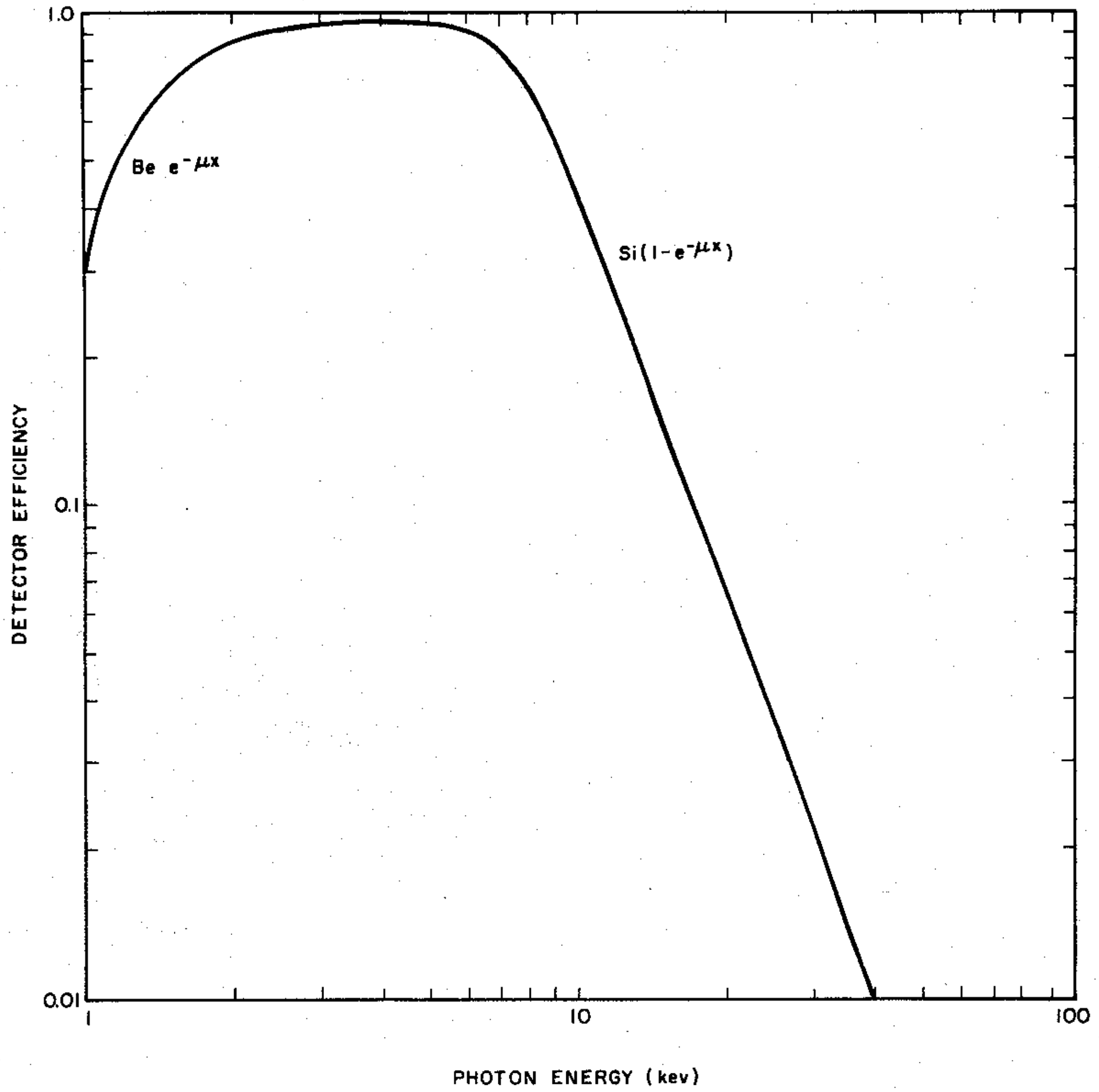

Figure 19. Calculated Efficiency of 75 μ Depleted Si Diode With 0.0005 Inch Be Window

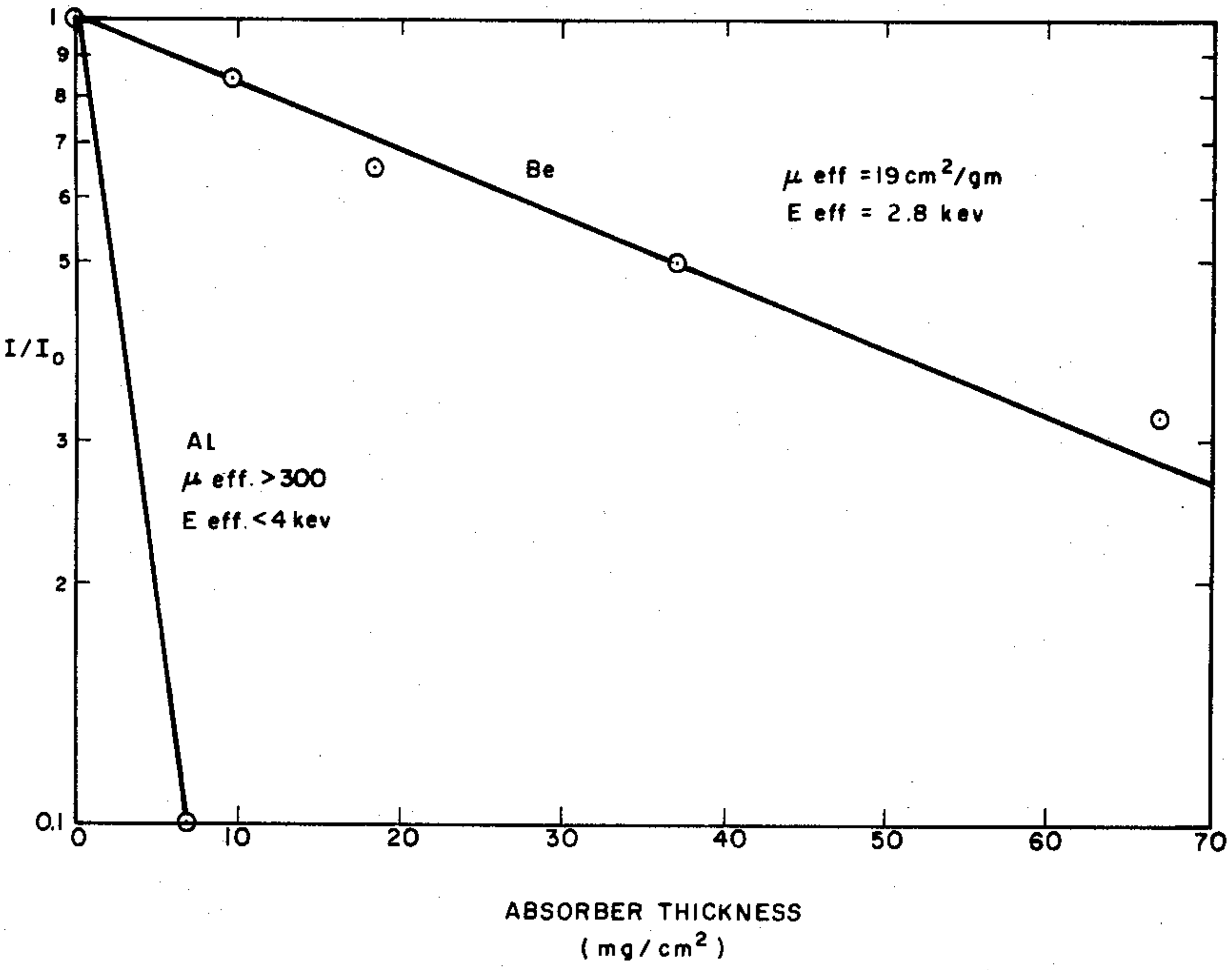

Figure 20. X-Ray Absorption Studies in Be and Al

1-2832

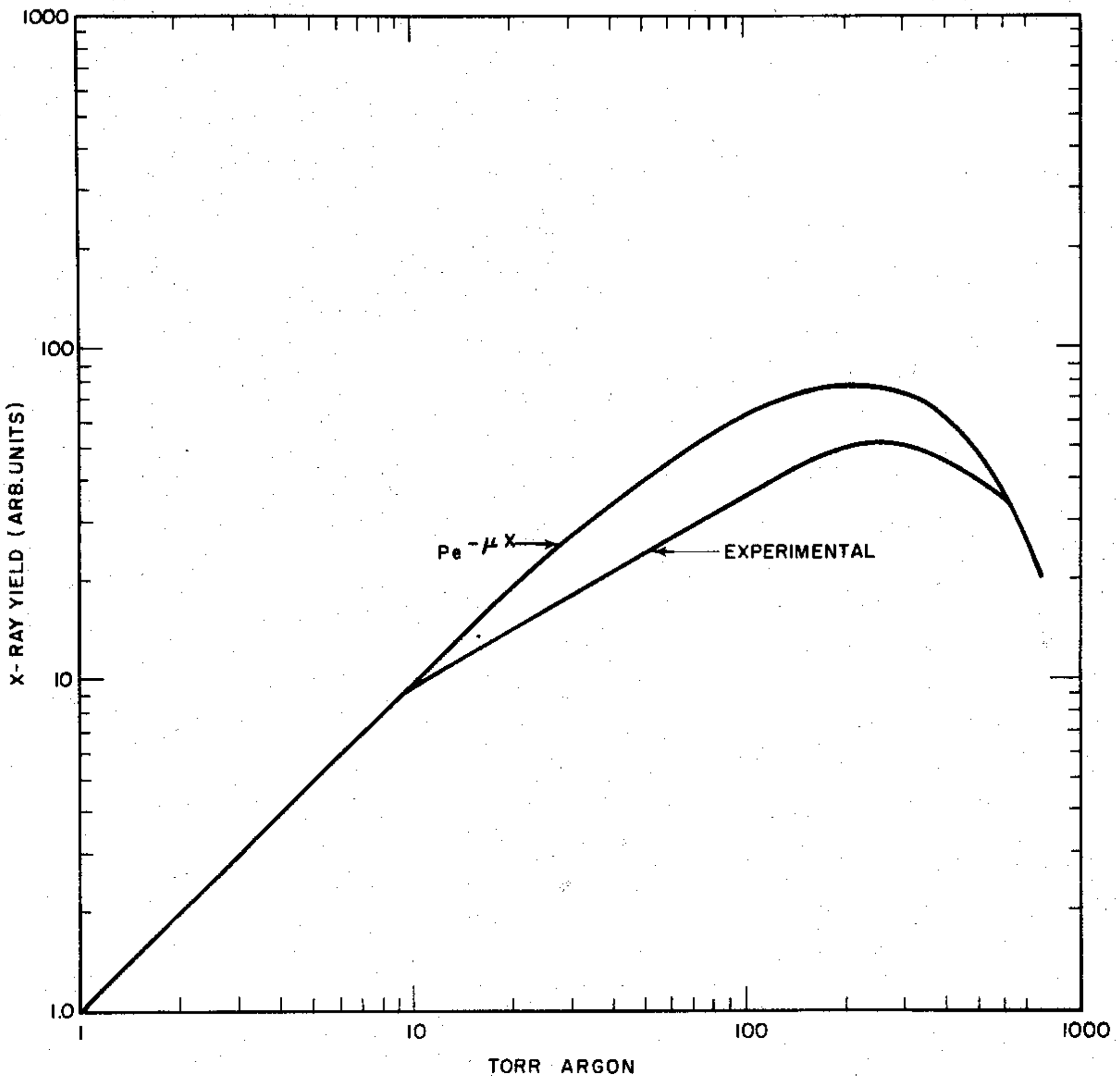

Figure 21. X-Ray Yield as a Function of Argon Pressure

1-2833

The proportion of incident radiation energy detected that is attributed to argon K emission can be measured by the critical absorption method. Absorber thicknesses can be set so that the attenuation is the same over a broad energy range except for the K edge region. We chose argon and chlorine as the two absorbers and designed a gas absorber chamber to do the experiment. (The chlorine was obtained by using CCl_4 vapor). The argon K ionization energy is 3.2 keV, the K-L photon is 2.95 keV and chlorine K ionization is 2.8 keV. We have then a 400 eV window in our 10 keV band or 4% of the detection bandwidth. The amount of radiation energy in the window will be:

$$\frac{\dfrac{I_1 - I_2}{I_o}}{e^{-\mu_1 (E_c) X_1} - e^{-\mu_2 (E_c) X_2}} = \frac{I(E_c)\,\Delta E_c}{\int_o^{E_{max}} I(E)\,dE}$$

where the subscripts 1 and 2 denote the absorbers, and E_c is the "critical" energy or the K edge energy. If the above relation gives an answer which is much greater than ~10%, then there is a strong indication of K line emission.

This function is plotted in Figure 22. The lower half of the figure shows the experimental points of the absorption experiments, (where the chlorine data has been adjusted by the 10% necessary to make the attenuation outside of the K ionization region match the argon), and the exponential functions corresponding to the absorption of argon K_α radiation. The top half of the figure shows the difference of these functions. The ratio of these is:

$$\frac{\dfrac{I_1 - I_2}{I_o}}{e^{-170X} - e^{-1700X}}$$

Which shows that at least 60% of the radiation is K emission.

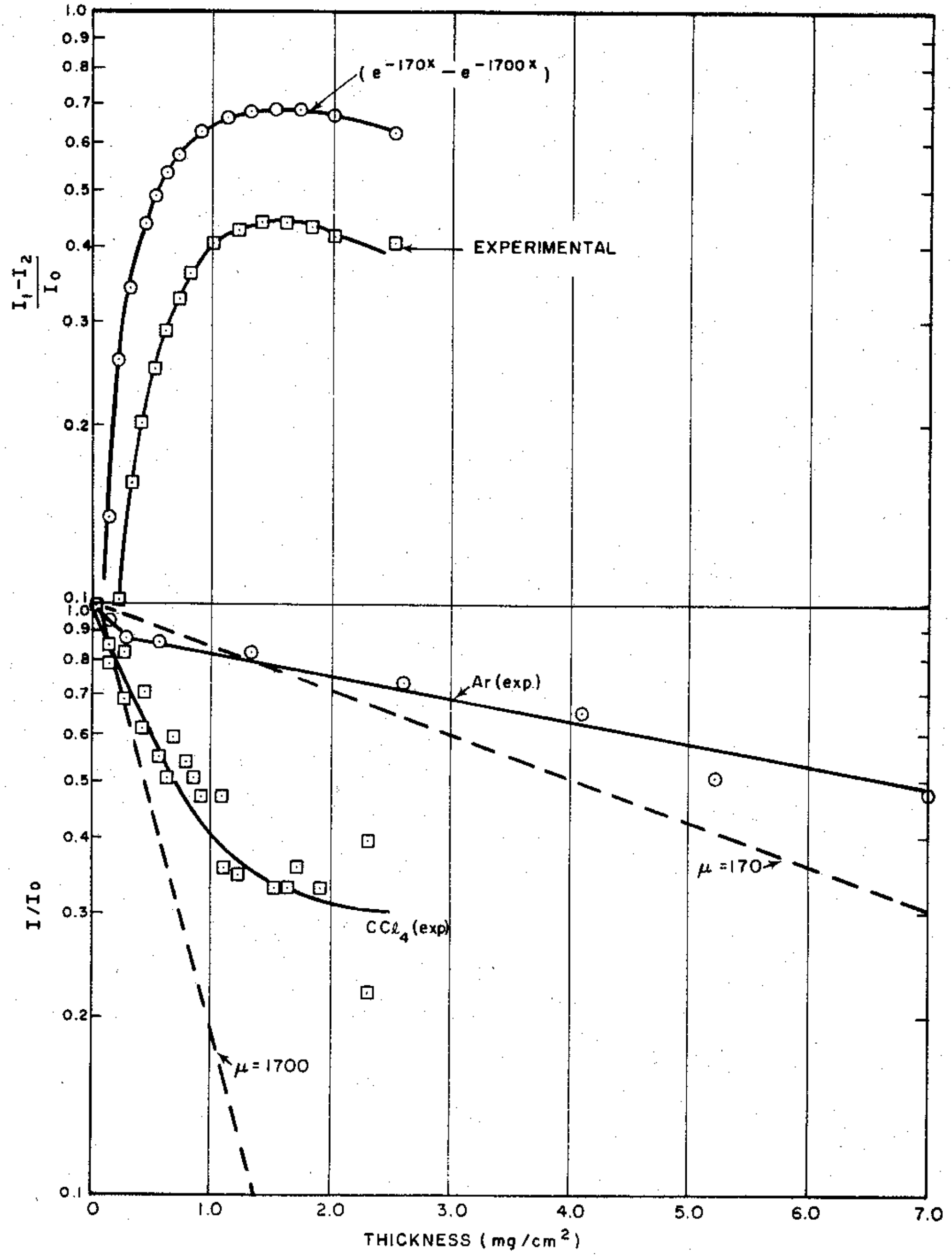

Figure 22. K Edge Absorption Results

1-2834

SECTION 3

ION ACCELERATION

3.1 Introduction

The presence of energetic ions in the plasma formed by the 30 ohm beam has been demonstrated by many measurements. These include the detection of D-D neutrons and their anisotropy, Be (p, n), (α, n), and (d, n) neutrons and direct detection of the ion current.

3.2 D(d, n) Neutrons

The detection of D(d, n) neutrons from the 30 ohm beam drifting in deuterium gas was discussed in Reference 1. This neutron yield is 10^9 per pulse at 0.15 torr as determined with the Los Alamos type moderated detector. The neutrons were also detected with the plastic phosphor-photomultiplier fast neutron detector as shown in Figure 23. The fact that they arrive in a fairly narrow burst (and are therefore nearly mono-energetic), tests with a bremsstrahlung target, and the magnetic analysis of the electron energy all confirm that these are (d, n) neutrons and not (γ, n) (2.2 MeV threshold).

The possibility of (e, n) neutrons was ruled out by stopping the ions with thin absorbers that transmitted the electron beam with negligible energy loss and noting the elimination of neutron production for both the D(d, n) and Be^9 (x, n) reactions. These experiments will be discussed later.

The anisotropy of the neutron yield from the 30 ohm beam passing through 0.15 torr of deuterium gas was first measured to be a 2/1 zero to ninety degree ratio. This was done with the moderated counter which is sensitive to scattered low energy neutrons. The experiment was repeated using the fast neutron detector which is insensitive to low energy neutrons. The results show a 3/1 zero to ninety degree ratio. Figure 24 shows the anisotropy compared to a $\cos^2 \theta$ curve normalized to the zero degree reading.(3) The longitudinal deutron energy needed to produce such an anisotropy is about 300 keV using the relationship given in Reference 3 of $(\sigma(\theta)/\sigma(0) - 1) = B(E) \cos^2 \theta$ and $B(E) = 0.31 + 0.006\, E_d$ where E_d is the deutron energy in keV.

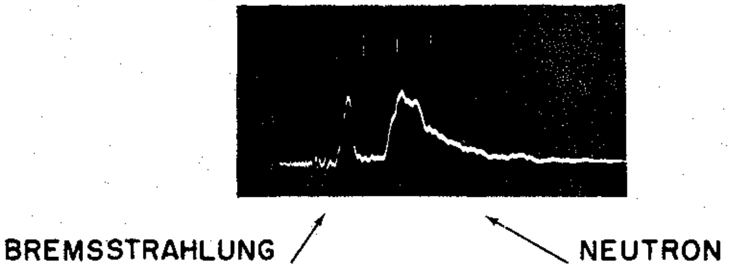

(a) Oscilloscope Trace

Vertical Scale 1 v/div
Horizontal Scale 100 nsec/div

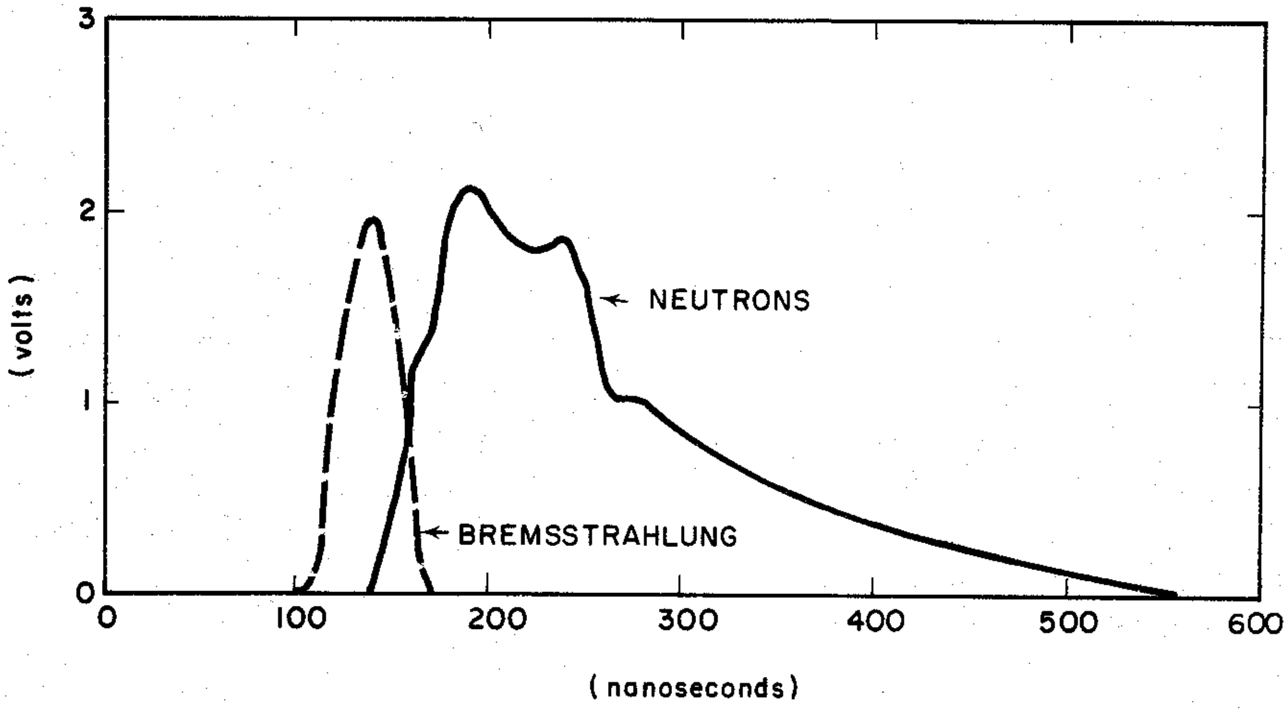

(b) Neutron Pulse with Time of Flight Subtracted

Figure 23 Production Rate of D-D Neutrons From Beam Plasma ($I/\beta\gamma$ = 10, 000)

2-823

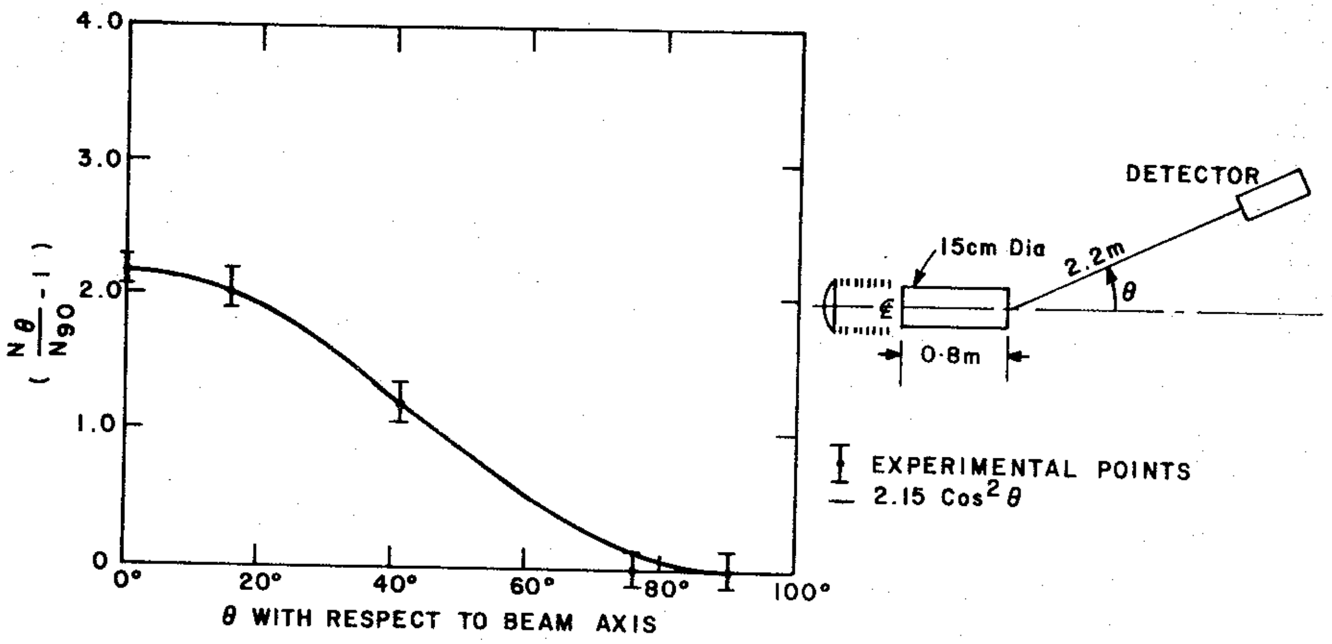

Figure 24 Neutron Anisotropy - 21 Needle Cathode
P-M Tube - Scintillator Detector

3.3 Be (x, n) Neutrons

The presence of energetic longitudinal ions was further confirmed by use of a Be target at the end of the drift section. Neutrons from the Be^9 $(d, n)\ B^{10}$, $Be^9\ (p, n)\ B^9$ and $Be^9\ (\alpha, n)\ C^{12}$ reactions were observed. A discussion of the yield versus pressure is deferred until the next section on the discussion of the time-of-flight data.

The matter of interest here is that the yields at optimum pressure were 2×10^9, 1.5×10^9 and 2×10^8 for the deutron, proton and helium ion studies. The Be^9 (p, n) reaction is of particular interest since the threshold energy is 1.8 MeV(4) and therefore it gives a lower limit for the proton energy. The Be^9 (d, n) yield sets a lower limit of 400 keV for the deuteron since below this the entire beam energy would have to be given to the deuterons to account for this yield of 2×10^9.(4)

3.4 Time of Flight Measurements

The ion energies were measured with a time of flight technique when it became evident that there was a longitudinal beam of ions. The experimental arrangement is shown in Figure 25. In these experiments the electron beam, after traversing 50 cm of the 6-inch diameter drift section, was deflected into the wall of the 1 inch diameter ion detection region. The ions with magnetic rigidities an order of magnitude greater than the electrons traversed the magnetic field with little deflection and were collected on a copper disc. The ion current was recorded on a Tektronix type 519 oscilloscope. The ion collectors were shown to have less than 1 ns time response with TDR analysis.

Figure 26 shows the current pulses resulting from passing beams through H_2, D_2, He, and N_2 gas. In each case the gas was admitted into an evacuated chamber and continuously pumped. The pressures were read with a McLeod guage.

The upper limit of pressure that was useable was 0.3 torr for all gases except N_2 which was limited to 0.05 torr. This limit was imposed by the diffusion of electrons through the magnetic field at higher pressures.

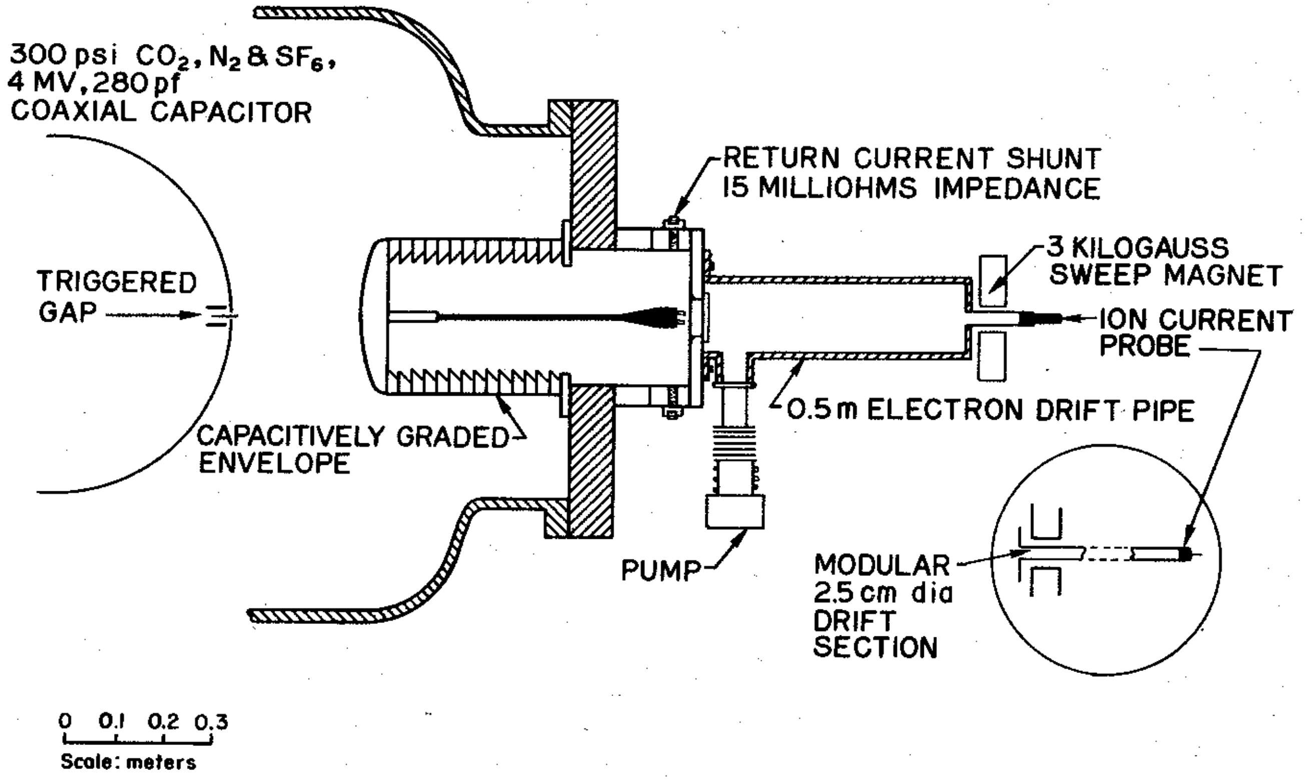

Figure 25. Experimental Arrangement for Beam Plasma Ion Detection

1-3462

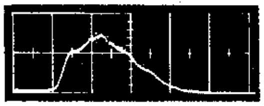

Entrance Current
31, 000 A/div
20 ns/div

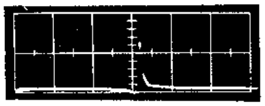

Ion Current
92 A/div
20 ns/div
0. 15 torr H_2

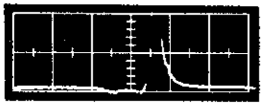

Ion Current
18. 4 A/div
20 ns/div
0. 15 torr D_2

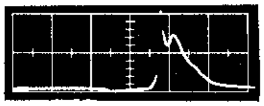

Ion Current
9. 2 A/div
20 ns/div
0. 20 torr He

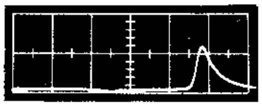

Ion Current
9. 2 A/div
20 ns/div
0. 25 torr N_2

Figure 26 Representative Ion Pulses

Pressures above these limits were investigated for energetic ions by use of the Be neutron reactions already discussed. It is seen in Figure 34 that either the ion flux or energy falls off rapidly above 0.300 torr. The next section of data analysis indicate that it is the flux that decreases.

The time of flight was measured by noting the position in time of the ion pulse relative to the current pulse at each of three longitudinal positions of the detector. In Figure 27 the technique is illustrated by representative proton data, 27(a) is the injection current pulse, 27(b) shows the proton pulse at the base position of the detector, 27(c) shows the pulse at the base position with the oscilloscope trigger delayed by a cable and the sweep speed increased from 20 to 10 ns/cm. Figure 27(d) and (e) show the result of adding 30 and 60 cm to the proton flight path. The results of these measurements are given in the next section.

3.5 Analysis of Longitudinal Ion Acceleration Studies

Analysis of the time of flight data for the various gas species studied consisted of lumping all pressure data together (which will be justified later), subtracting out the time of arrival at the "zero" position at each pressure and then plotting the data on a time versus distance graph. In all cases the arrival time at a given position was taken to be the leading edge of the ionic current pulse. It is apparent on this type of plot that there does not seem to be any dependence of the ion energy on pressure, and in fact the scatter in the data is roughly what one would expect from statistical fluctuations.

The results of the analysis are shown in Figures 28, 29, 30 and 31. Figure 28 is the data for hydrogen, and indicates that the velocity and energy of the protons are:

$$\beta = \frac{v}{c} = 0.10 \pm 0.01$$

$$E = \frac{1}{2} (M_H C^2) \beta^2 = 4.8 \pm 0.9 \text{ MeV}$$

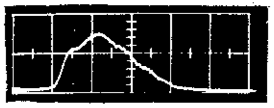

Entrance Current
31, 000 A/div
20 ns/div

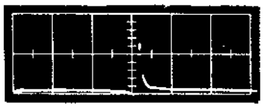

Proton Current at Defined
Zero Position
92 A/div
20 ns/div

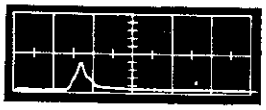

With Trigger Delay at
Defined Zero Position
92 A/div
10 ns/div

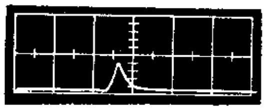

30 cm Drift
18 A/div
10 ns/div

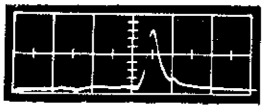

60 cm Drift
4. 6 A/div
10 ns/div

Figure 27 Representative Proton Flight Time Data

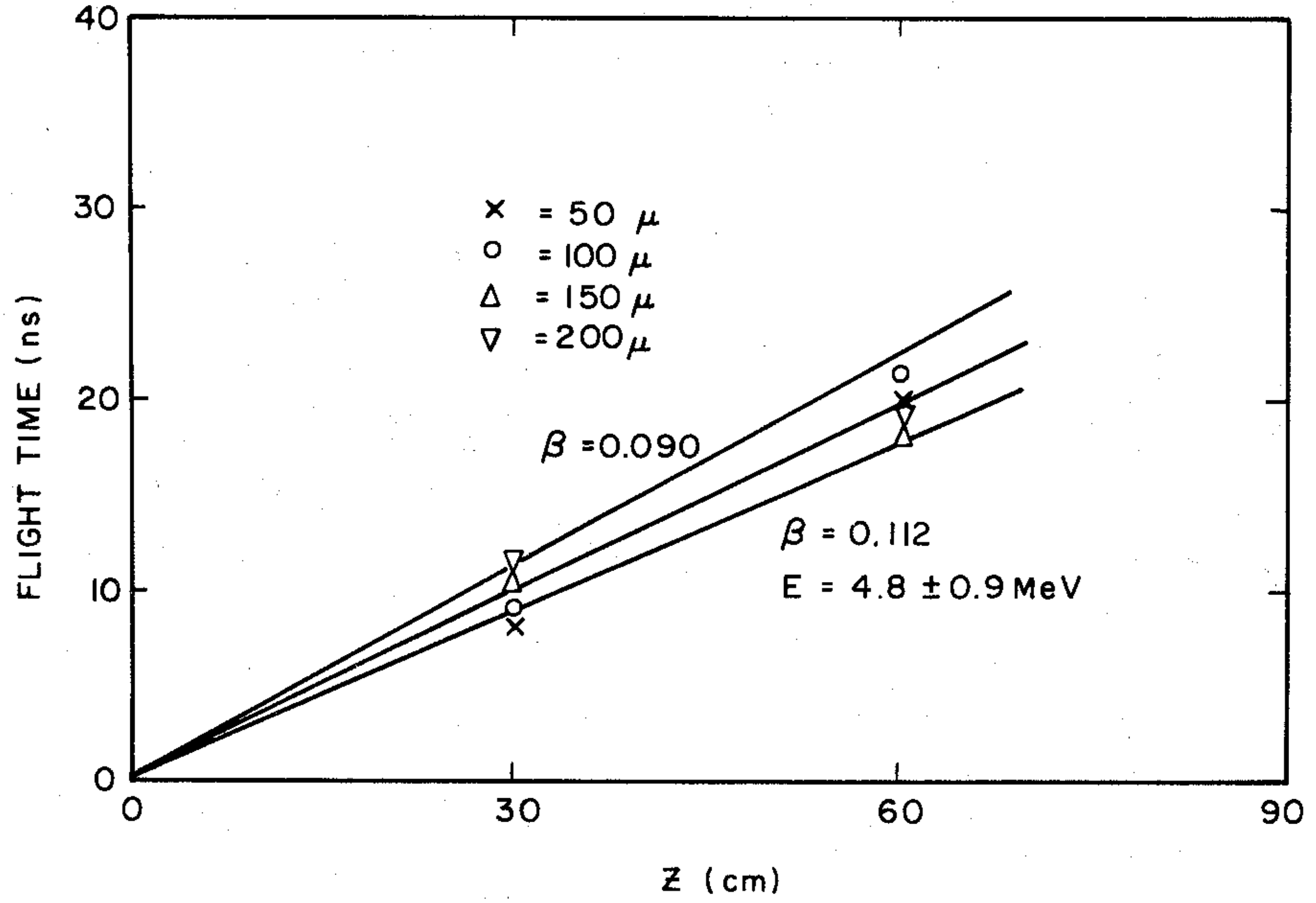

Figure 28. Time-of-Flight Data for Hydrogen Ions

1-3463

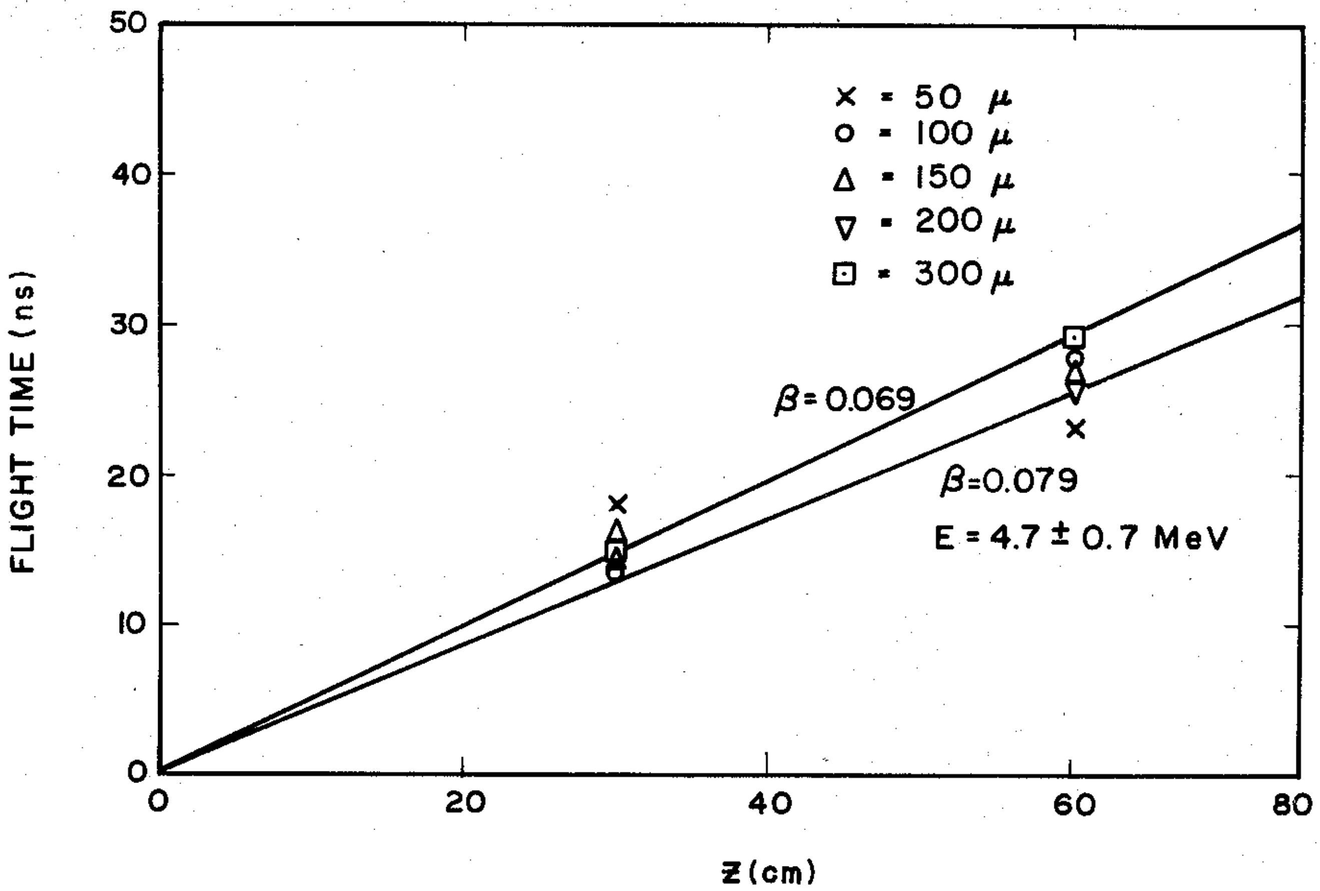

Figure 29. Time-of-Flight Data for Deuterium Ions

1-3464

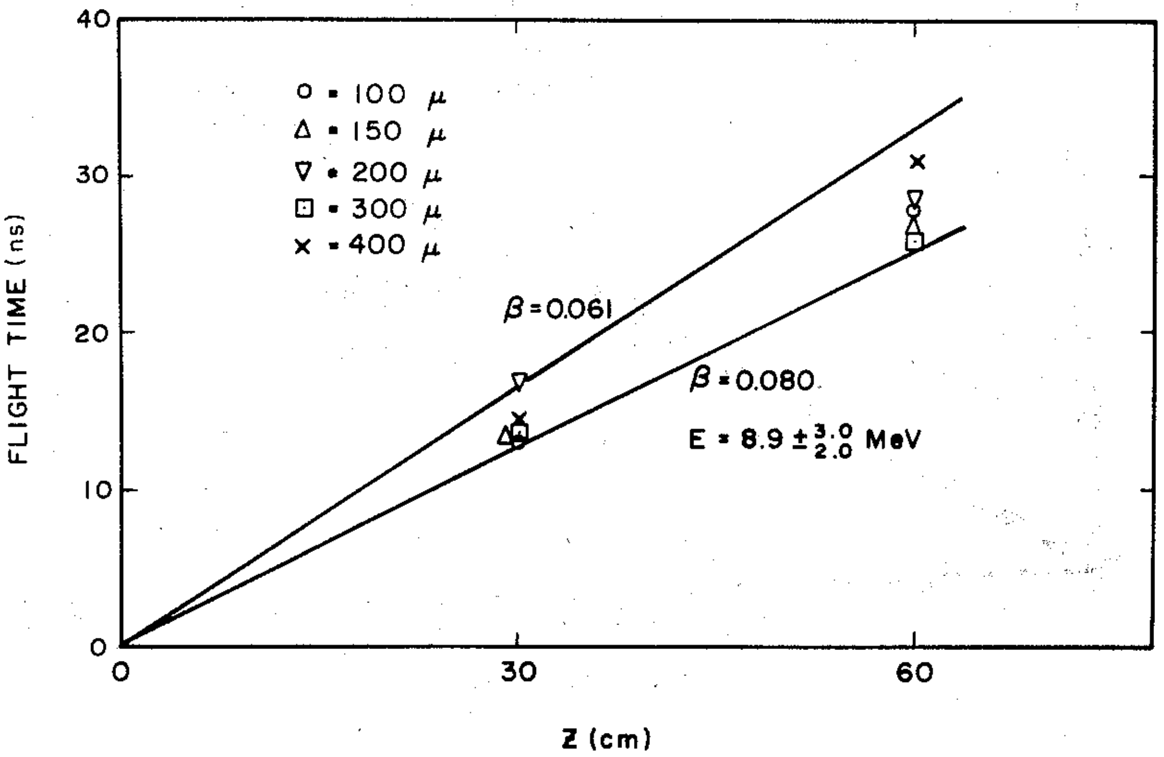

Figure 30. Time-of-Flight Data for Helium Ions

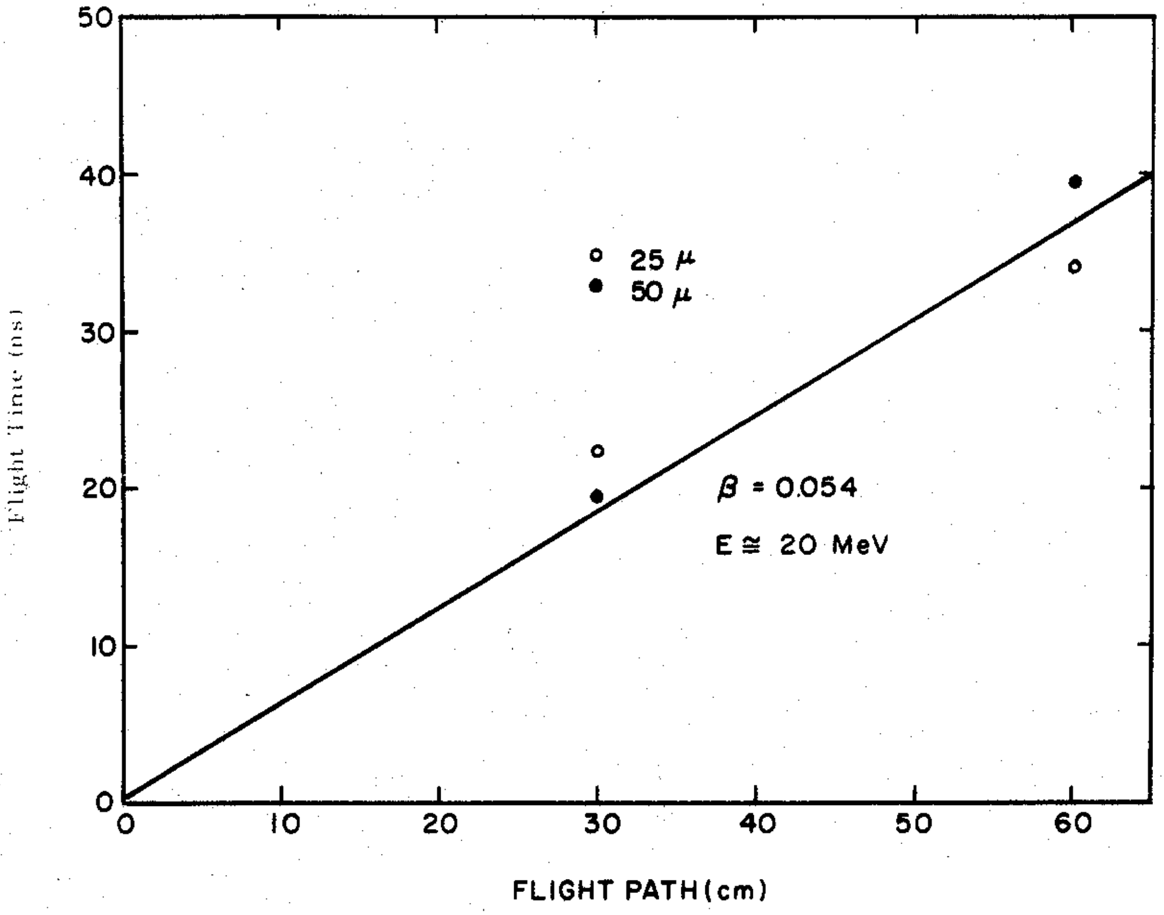

Figure 31. Time-of-Flight Data for Nitrogen Ions

1-3466

Figure 29 shows the deuterium data, and gives:

$$\beta = 0.074 \pm 0.005$$

$$E = 4.7 \pm 0.7 \text{ MeV}$$

Figure 30 presents the data for helium, and gives:

$$\beta = 0.07 \pm 0.01$$

$$E = 8.9 \begin{matrix} + & 3.0 \\ - & 2.0 \end{matrix} \text{ MeV}$$

Finally, Figure 31 gives the data for nitrogen. The amount of data is much less in this case, and the scatter is rather bad. Roughly, one obtains:

$$E \approx 20 \text{ MeV}$$

The striking feature is that for H_2, D_2 and He the ion energy seems to depend only on the atomic charge of the species. Thus:

$$Z_{H_e} = 2 Z_H$$

and:

$$E_{He} \simeq 2 E_H$$

This extrapolation breaks down for nitrogen, indicating that the ions are not completely stripped. Assuming that the ion energy is directly proportional to the degree of ionization, the data indicates the nitrogen to be 4 or 5 times ionized. This is consistent with time-resolved spectroscopic measurements of the plasma line radiation, which shows N^{V} and N^{VI} lines appearing early in time.

To get some feeling of how the ion energy scales with beam current, a series of runs were made on hydrogen, keeping the gas pressure constant (at 150 μ) and varying the charging voltage on the coaxial PFN. Since the cathode was observed to be a constant impedance, this is equivalent to varying the beam current (or energy). The results are shown in Figure 32, and indicate that a good fit to the data is:

$$E_p \propto I^2$$

A collective acceleration model would predict such a relationship, while a space charge model would give a linear dependence on current, so that the collective model is favored on this basis.

An important difference between the models arises if one considers how the ion energy depends on ionic charge. The relations are:

(a) collective model(7)

$$E \propto Z^2$$

(b) space charge model

$$E \propto Z$$

On these grounds, the data tends to support the space charge model.

Figure 33 shows the absolute time of arrival (referring to the beginning of the beam current pulse as t = 0), at various detector positions, as a function of pressure for hydrogen. One might expect that no acceleration mechanism would be operative until the primary electron beam begins to pinch. The time it takes to develop enough plasma to force neutralize the beam is given by:

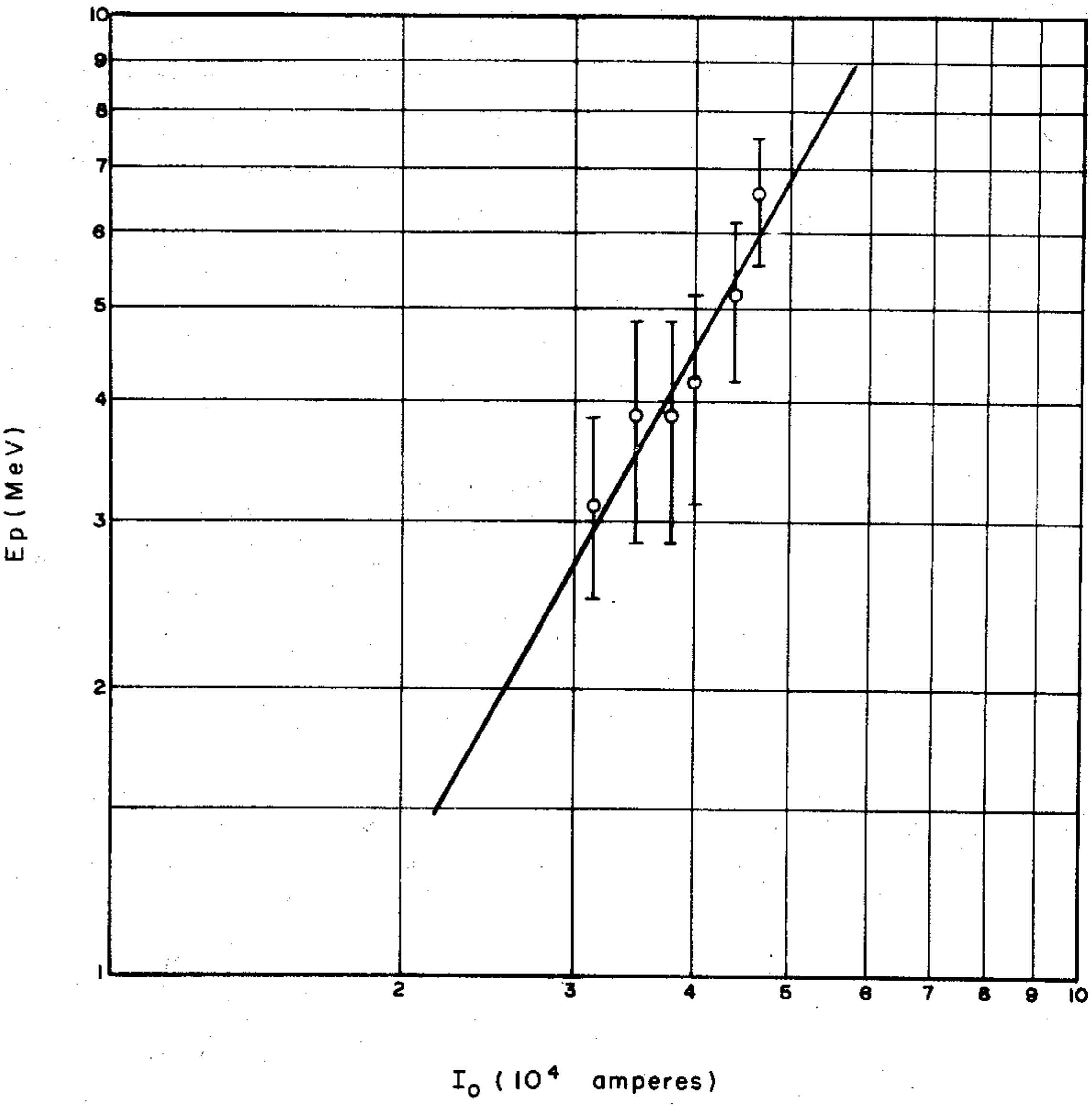

Figure 32. Dependence of Hydrogen Ion Energy on Primary Beam Current

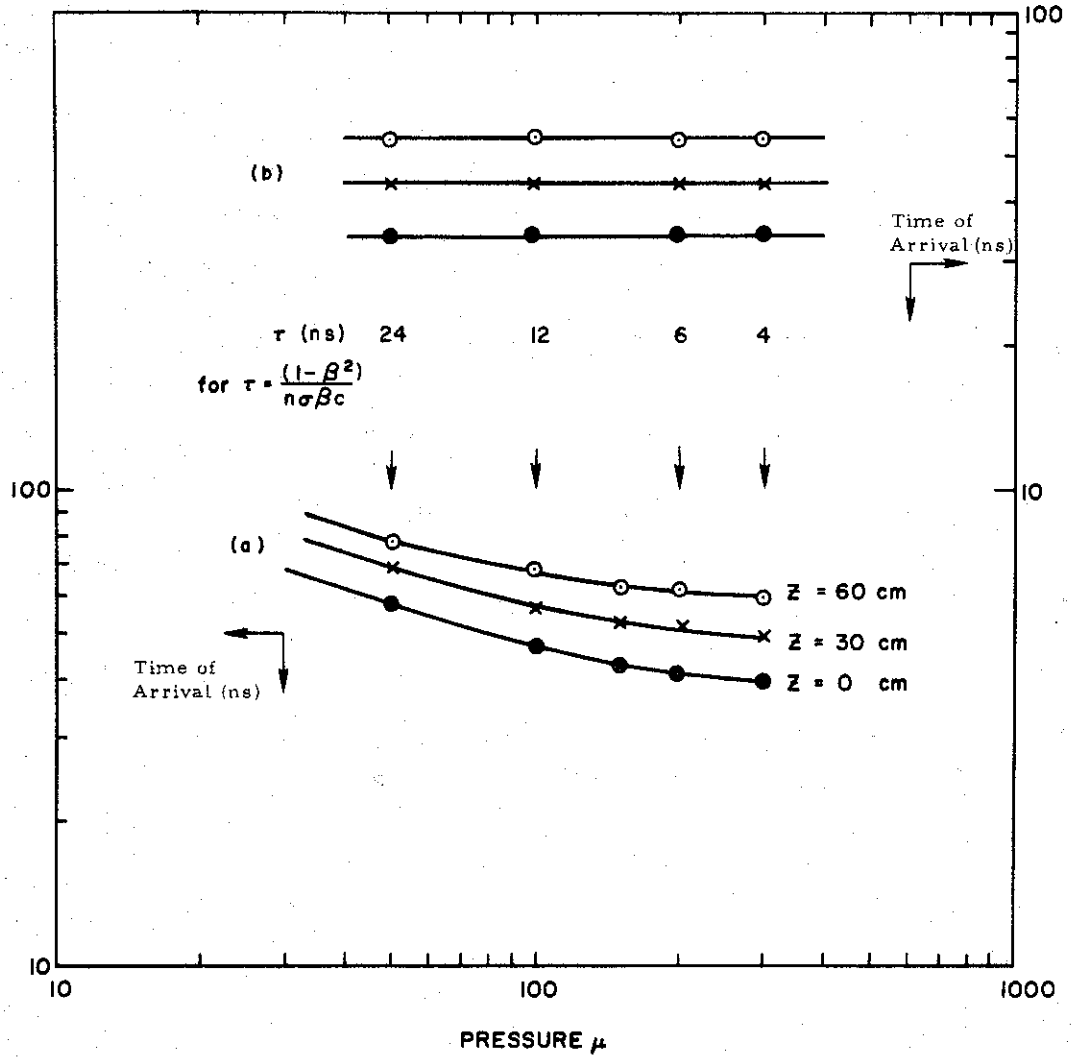

Figure 33. Dependence of Hydrogen Ion Arrival Time on Ambient Pressure

$$\tau = \frac{(1 - \beta^2)}{n_o \beta c \sigma}$$

where:

n_o = ambient gas density $\propto$ pressure

σ = ionization cross-section = 10^{-19} cm^2 for H_z

β = primary electron velocity.

For a 1.25 MeV electron beam in hydrogen, the appropriate numbers are:

τ (p = 50 μ) = 24 ns

τ (p = 100 μ) = 12 ns

τ (p = 200 μ) = 6 ns

τ (p = 300 μ) = 4 ns

If the data in Figure 33(a) is corrected by subtracting out the time it takes before the beam begins to pinch, one obtains the results shown in Figure 33(b). The result is striking, and indicates that the arrival time of the accelerated ions at a given detector location is independent of pressure if the time is measured from the beginning of the beam pinch. This also indicates that the ion energy is independent of pressure. Note that the space charge is not neutralized, so that at first sight this behavior does not favor one acceleration mechanism over the other.

Another parameter of interest is the total amount of charge which is accelerated at a given ambient pressure. The charge collector measurements are not particularly good indicators of this, since the amplitude of the detected signal depends strongly on the exact spatial motion of the primary beam.

Since this is not highly reproducible, an alternate measureing scheme was used. This was the Be target neutron production mentioned previously. The target was placed in the end of the dirft tube and the reactions Be^9 (p, n) B^9, Be^9 (d, n) B^{10}, Be^9 (He, n) C^{12} and the D(d, n) He^3 in deuterim gas were monitored. The yields of these reactions are shown in Figure 34. Since the ion energies have been shown to be independent of pressure, the neutron yield is a measure of the total charge striking the beryllium target. For these conditions the yields are about a microcoulomb for deuterons and protons and about 0. 1 μ C for the helium ions.(4)

The total charge delivered will be a complicated function of pressure, since the number of ions available for acceleration will increase linearly with pressure, the time available for acceleration will vary inversely with pressure ($\tau = T_o - A/P$), and the scatter mean free path will vary inversely with pressure. Qualitatively, the curves show the charge delivered increasing with pressure as more ions become available until it reaches a fairly broad maximum, and then presumably the scattering effects dominate and the total charge delivered begins to decrease.

The proton energy was further confirmed with beryllium absorbers and the current detector. The extrapolated range was shown to be about 50 mg/cm^2 of Be which corresponds to 5. 5 MeV protons which is in excellent agreement with the rest of the data.

Figure 35 summarizes the longitudinal ion data.

Protons moving in the radial direction have been detected. These are more abundant at low pressure, 0. 05 torr, where they are observed near the window and with an energy of about 1 MeV. At 0. 150 torr radial protons are observed at the far end, Z = 50 cm, with about 1 MeV of energy. The system for this measurement consisted of two solid state detectors charge collectors as shown in Figure 36.

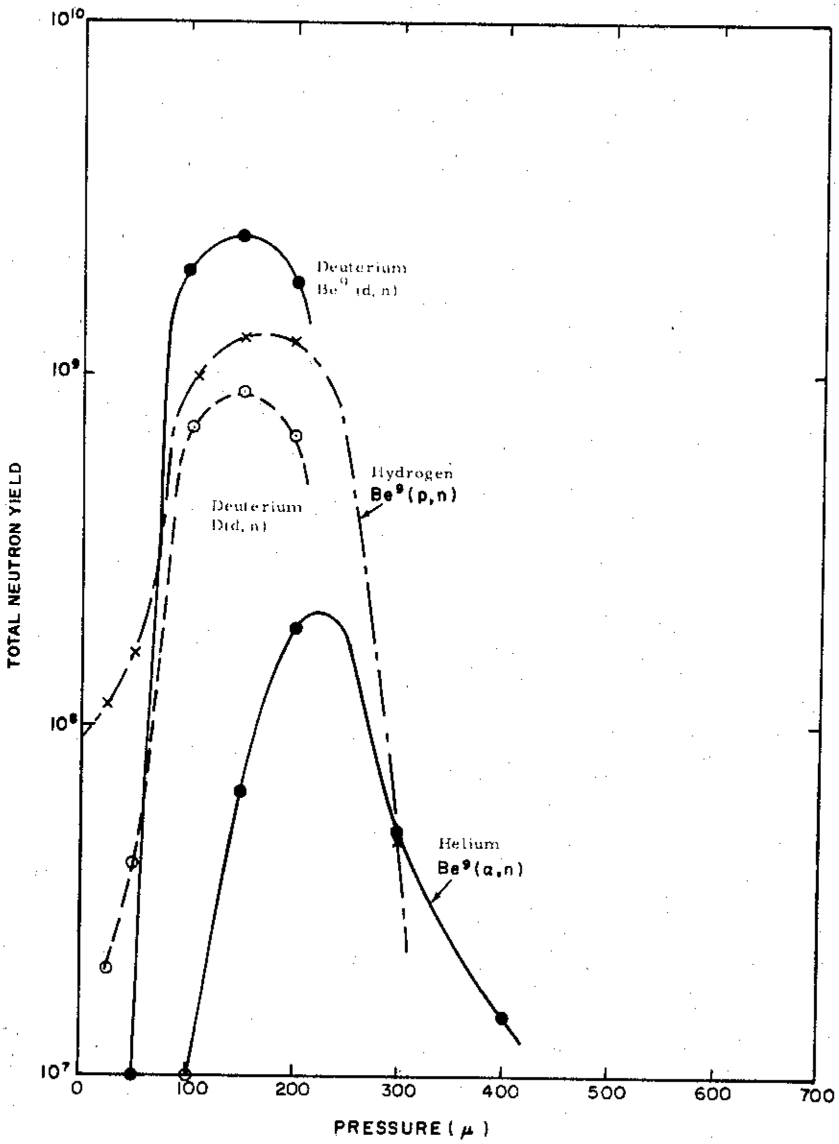

Figure 34. Total Neutron Yields for the Reactions Be (x, n) and D(d, n) as a Function of Filling Pressure

Pressure	25 μ	50 μ	100 μ	150 μ	200 μ	300 μ	400 μ
Hydrogen							
I (A)		9	100	100	100		
τ (ns)		15 ns	3 ns	3 ns	3 ns		
E (MeV)		4.8 ± 0.9 MeV	4.8 ± 0.9 MeV	4.8 ± 0.9 MeV	4.8 ± 0.9 MeV		
Deuterium							
I (A)		9	30	80	50	12	
τ (ns)		8	5	5	3		
E (MeV)		4.7 ± 0.7 MeV	4.7 ± 0.7 MeV	4.7 ± 0.7 MeV	4.7 ± 0.7 MeV	4.7 ± 0.7 MeV	
Helium							
I (A)			2.0	8.0	20	20	8
τ (ns)			40	10	7	7	5
E (MeV)			$8.9^{+3.0}_{-2.0}$ MeV	$8.9^{+3.0}_{-2.0}$ MeV	$8.9^{+3.0}_{-2.0}$ MeV	$8.9^{+3.0}_{-2.0}$ MeV	$8.9^{+3.0}_{-2.0}$ MeV
Nitrogen							
I (A)	14	10					
τ (ns)	15	8					
E (MeV)	20.0 MeV	20.0 MeV					

Figure 35. Summary of Energetic Ion Data

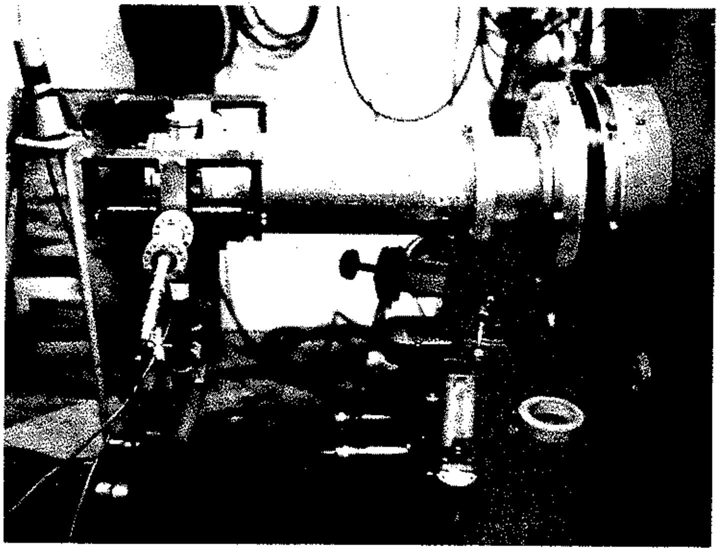

Figure 36. Typical Radial Ion Detection System

3.6 Acceleration Region Determination

Although the acceleration mechanism is not understood at this time, some experimentally observed phenomena are at least self consistent. The acceleration length and the origin volume of the energetic ions is known.

The length required for ion acceleration is about 30 cm as ascertained by several measurements:

(a) the D(d, n) neutron yield as a function of drift tube length

(b) the Be (d, n) neutron yield as a function of window to target length

(c) the D(d, n) yield with a thin (3.5 mg/cm^2) cellophane sheet placed in the beam which stops about 1 MeV ions but not the energetic electrons.

These results are plotted in Figure 37 where it is seen that 20-30 cm is needed for ion acceleration with this beam. In another experiment where the drift tube was covered with paraffin except for a circumferential slot, the neutron yield was measured with the fast neutron detectors with the slot at different longitudinal positions. The result was that most of the neutron production was from 30-50 cm as seen in Figure 38.

With end collimation of the neutrons and by masking the Be target it was ascertained that the ions are contained in the electron beam and that the variance of pulse height (ion current) in the detectors is due to beam wonder (this masking of the Be target also ruled out (γ, n) and (e, n) neutrons as a source).

In conclusion then, the fact that there are energetic (Mev) ions is conclusively proved and the necessary acceleration length seems to be about 30 cm.

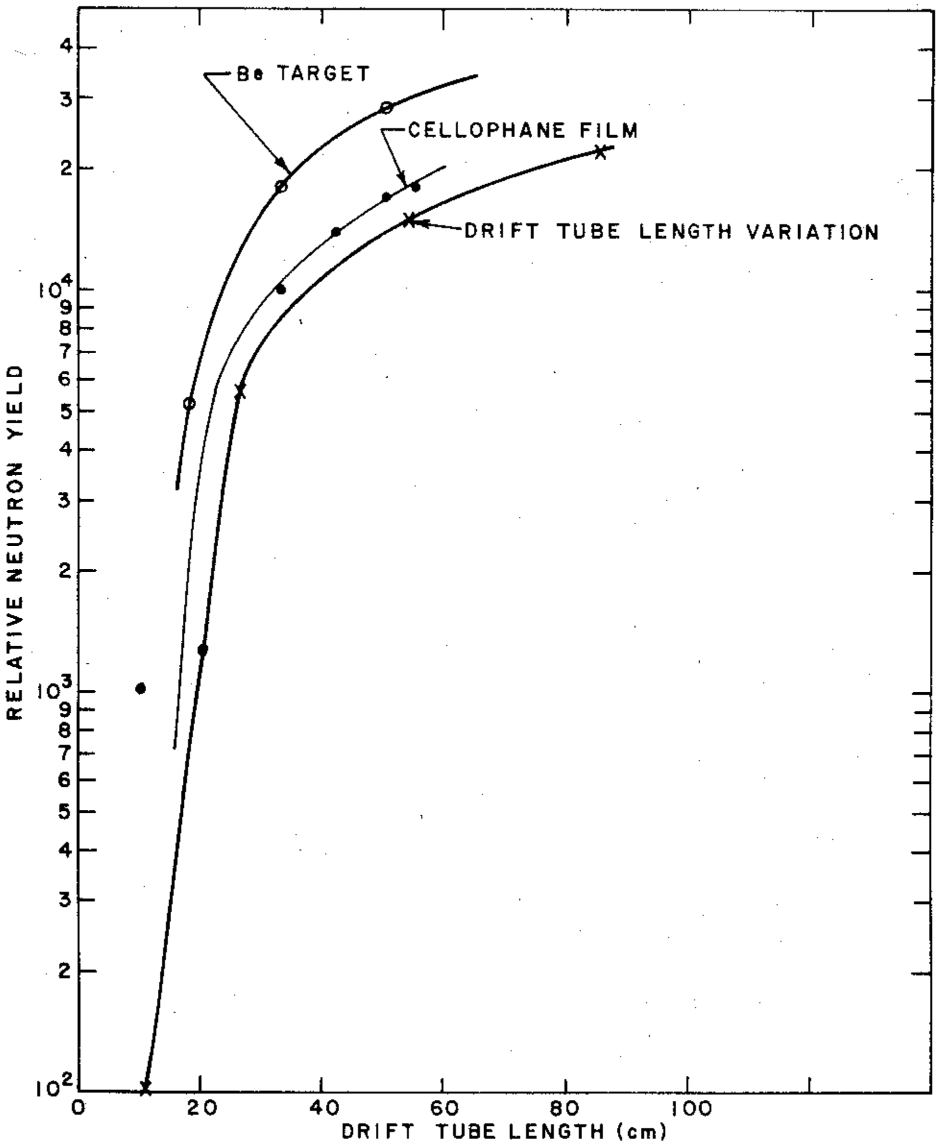

Figure 37. Measurement of Ion Acceleration Length
20 Pin Cathode, 30 ohm Gap

1-3591

1-3592

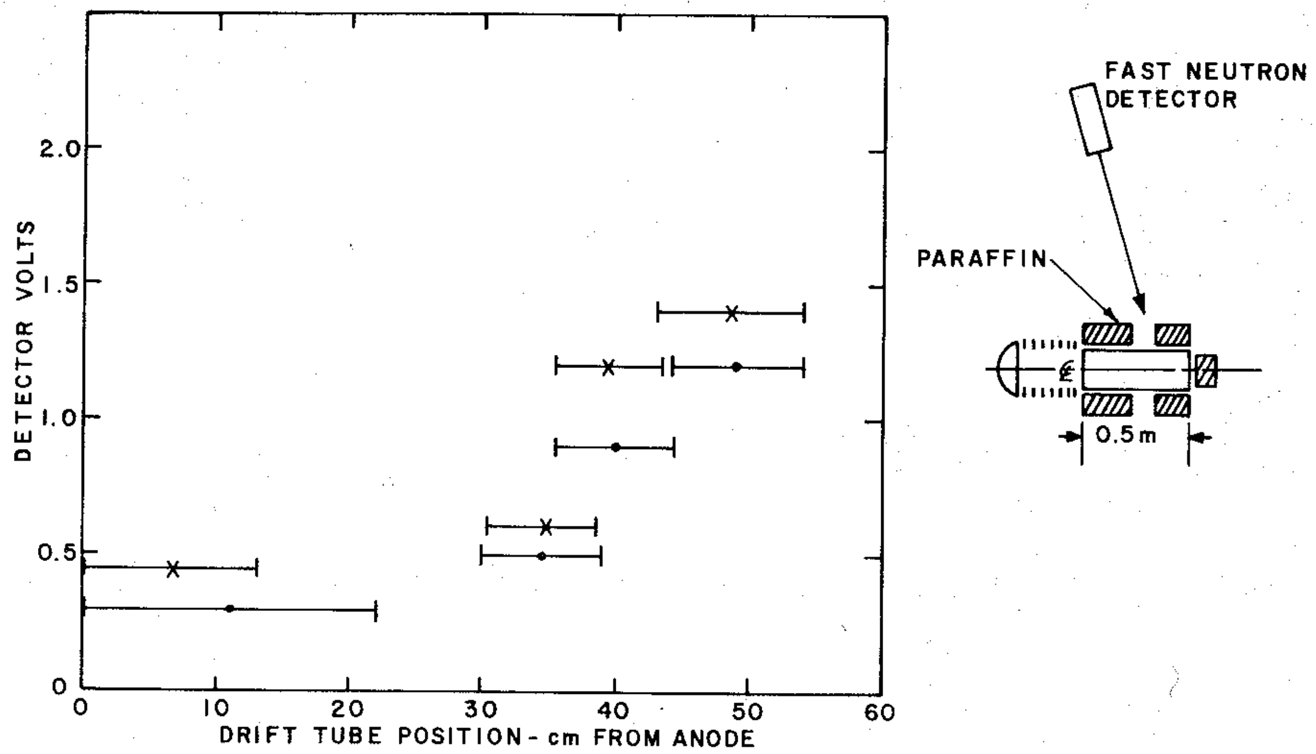

Figure 38. Radial Collimation of D(d, n) Neutrons

SECTION 4

OPTICAL AND SPECTROGRAPHIC DIAGNOSTICS

4.1 Review

Under the first phase of Contract DA-49-146-XZ-553, the application of 1500 J self-focused, 1.5 MeV electron pulses of 25 ns duration to a production of energetic plasmas was studied by time resolved emission spectroscopy.(1) In argon and helium, at pressures of from 0.15 torr to 1.5 torr, high energy plasmas were formed which continued radiating for up to 500 μs. Under drifting electron beam conditions(5) the helium plasma appeared to be doubly ionized. The light peaked early and late and showed a minimum, with plasma instability effects at intermediate times. Measurements of excitation temperature from the relative intensities of neutral helium lines fit an equilibrium model 2 μs after the electron passage and indicated a temperature of 14,000°K falling to 4000°K by 400 μs. At 0.60 torr drift chamber pressure, a measurement of electron density from the width of the HeI 4921 Å line showed an electron density of 1.2×10^{15} cm^{-3} at 70 μs falling to 3.4×10^{14} cm^{-3} by 200 μs. Studies of an argon plasma showed the emission at peak excitation density to be in the argon IV spectra. It was previously shown that when the beam exceeds the "Lawson Limit" it is stopped by its own magnetic compression.(6) When this is used as an ionization and heating mode in argon, the plasma was seen to reach an energy which is high compared to the 145 eV necessary to four times ionize, and it remained above this level for 8 μs.

4.2 Introduction

In the second (current) phase effort, the development of multi-pin and plasma cathodes to form propagating electron beams of $\nu/\gamma > 1/2$ has determined the types of spectral diagnostics which should be further developed. The plasmas produced by such beams have proved to be so energetic and so sensitive to beam parameters as to make further studies of the very late equilibrium plasmas unrewarding. The cavity techniques used to observe non-equilibrium transitions in the early time plasmas showed non-thermal populations persisting into late times.

Studies of axial light signatures of higher levels of ionization have shown progressive heating through the ionization levels of oxygen and nitrogen leading to complete ionization. At late times, progressive recombination through the levels was observed. Hydrogenic transitions of He II, N VII and O VIII have been easily observed.

Broadening and splitting of spectral lines has been observed as a function of time in the plasma. The mechanisms responsible are not understood, but the magnitudes of the effects appear to be dependent on electron beam parameters.

4. 3 Optical Cavity Studies

It has been shown that a non-equilibrium plasma can be produced by pulsed relativistic electron beams, and that the plasma can stay in non-equilibrium states for a considerable time. The characteristics of such a plasma can be investigated by measuring the population inversion produced. This is done by producing the plasma in a cavity and stimulating the relaxation of certain levels.

A system to allow introduction of the electron beam into an optical cavity is shown in Figure 39. A cathode configuration (a) and cathode-to-anode (foil window) gap (b) was chosen to allow the major part of the electron beam to pass around a carbon shield (c) and a cavity mirror (d) before pinching. Electrons which drift downstream are swept to the walls by a magnet (e). This protected the downstream, partially transmitting, cavity mirror (f) and the exit window. All optics were quartz. Ten spectral transitions of one, two and three times ionized argon were observed. The lines chosen have been observed in stimulated emission in other plasmas, and arise from known transitions.

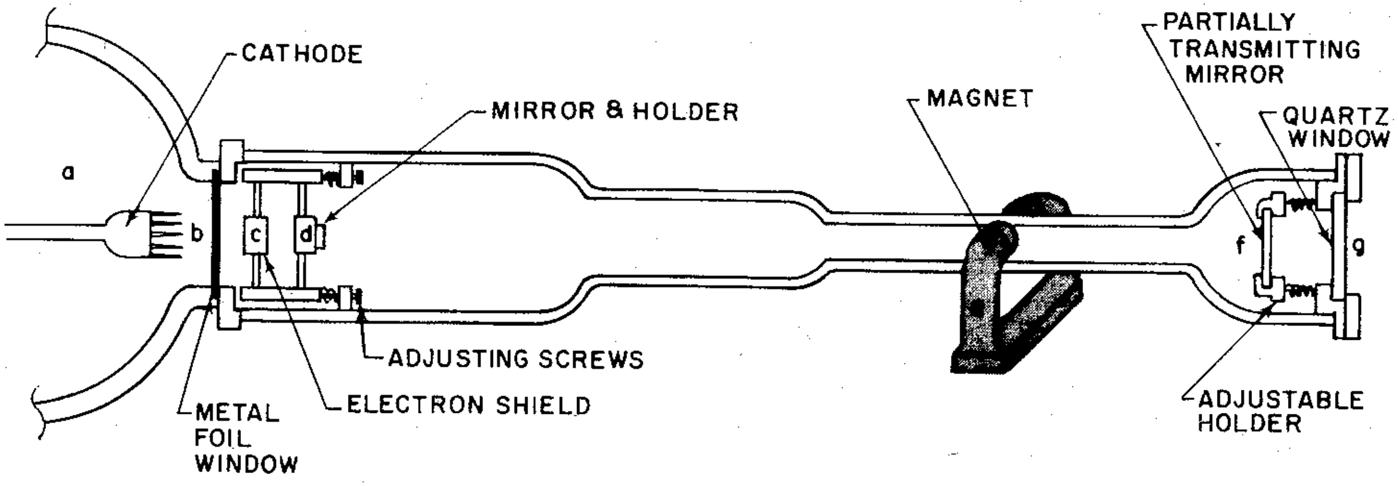

Figure 39. Electron Beam Pumped Optical Cavity

An 0. 5 m Jarrel Ash monochromator was used to measure the time history of the parallel axial emission of these ten lines with the cavity aligned and with the foreward mirror removed and the downstream mirror turned a few degrees. As only one line could be observed at a time, three pulses were taken each time. A series of spectral lines was examined from Ar II, Ar III, and Ar IV. The lines were chosen from a list of known laser lines.(8)

The amplification (the ratio of the intensity of a line with the cavity to the intensity without the cavity) is shown in Figure 40 for nine lines, as a function of time. In each case, the appearance of stimulated emission was also accompanied by an increase in noise and an increase in the variation of the traces between pulses.

From Figure 40 it can be seen that the Ar IV transitions (solid lines) peak early in the pulse. The Ar III transitions (dashed lines) peak late in the pulse and the Ar II transitions (dotted lines) show peaking both early and late. Three of the lines show no appreciable amplification. The tenth line, the 3511 Å Ar III line, was the brightest of all the observed lines and showed a time behavior similar to the other lines when the cavity was aligned, but gave inconsistent results. This transition has been observed to be super-radiant in other discharges. That is, it was seen to lase with or without cavity mirrors. That possibly also happens here.

None of these first choice configurations (i. e. multiple pin cathode, flat mirrors, adjustment and alignment system, tube length) or choice of the transitions appear to be optimum, but amplification and therefore population inversion have been shown to occur.

It can be concluded that relativistic beam produced plasmas can be diagnosed by population inversion techniques.

4. 4 Highly Ionized Line Signatures

The long times at which population inversions were seen among the first few levels of ionization showed that higher levels of ionization would have

1-2829

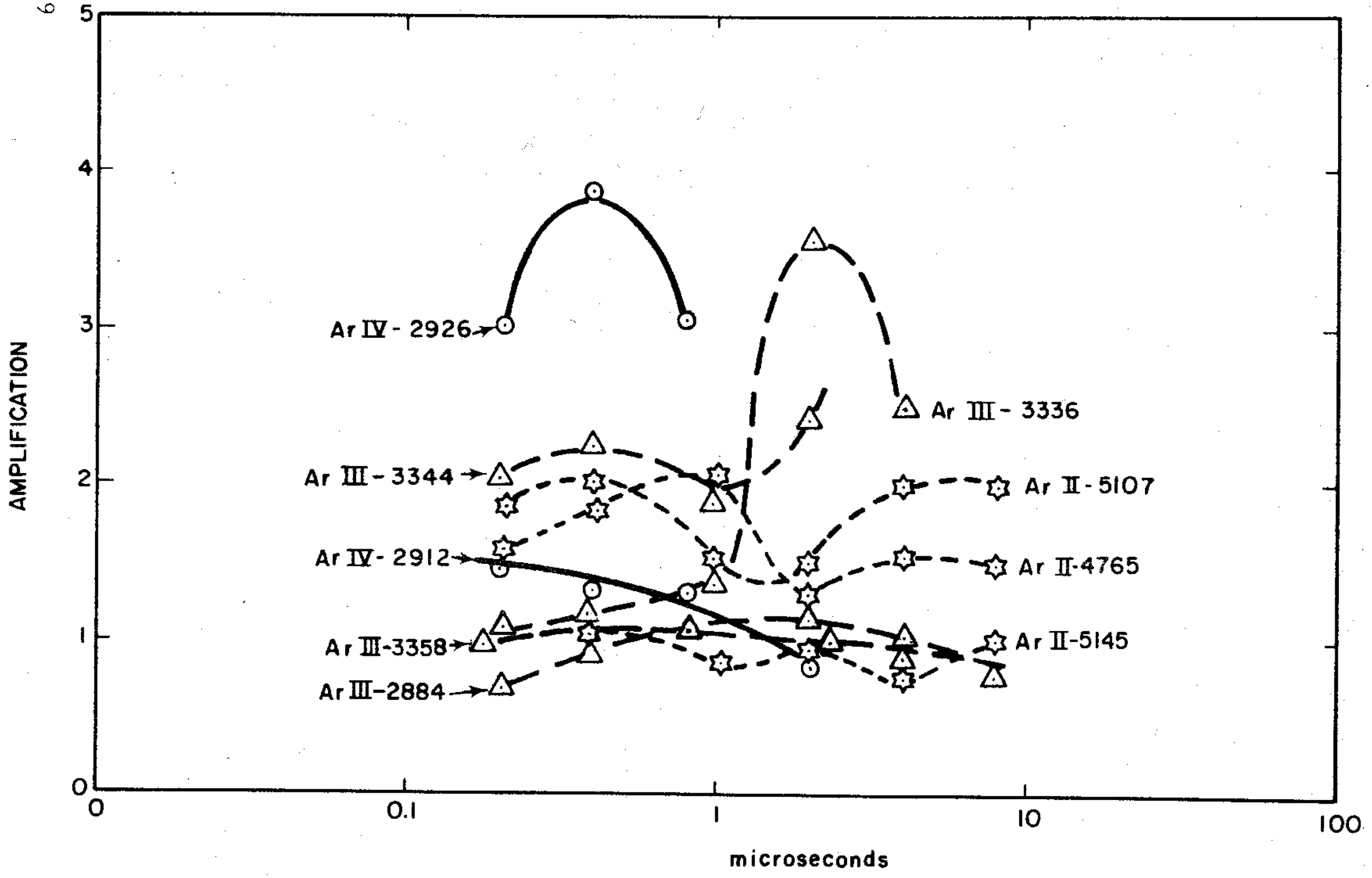

Figure 40. Electron Beam Produced Plasma Stimulated Emission (p = 150 μ)

to be investigated in order to estimate the energies and densities which occur early in the plasma formation.

The spectral range of the 0.5 m vacuum monochromator was extended downward to 1850 Å by use of vacuum techniques. It has been found to be practical to operate with the monochromator approximately 6 ft from the FX-25 accelerator (and on the beam axis) by appropriate shielding. The monochromator was set up and shielded on an adjustable steel table and connected to the drift tube by 1-inch diameter aluminum tubing. It was found necessary to electrically separate the monochromator from the drift tube. The arrangement is shown in Figure 41. The instrument was protected by a magnet near the end of the drift pipe to sweep electrons to the wall, and by a quartz window at the entrance slit. The window also allowed the monochromator and drift tube to be at different pressures. The monochromator was evacuated with a diffusion pump and a liquid nitrogen trap. The photomultiplier extended into the evacuated region using an O-ring vacuum seal.

The monochromator slits were set at 100 μ, defining a resolution of 1.6 Å. The instrument could be accurately set to 0.5 Å and stepped in 0.1 Å increments. Wavelengths of selected transitions were taken from the National Standard Reference Series of the National Bureau of Standards.(8) They were chosen to be among the brighter transitions which represent different regions of the energy levels of the various ions. A sample trace of the time resolved signature of a typical line of each observed ionization state of oxygen is shown in Figure 42. A general trend can be seen in terms of shortening the length of the dark "ionized" regime. The total length of the pulse can be seen to progressively shorten as higher levels of ionization are observed. This trend is detectable but is not a strong enough effect to make a characteristic signature for each ion, as was previously observed for the focused propagating electron beam mode. The signatures vary quite a bit among the lines of each ion. Some lines show the typical signature expected of a different level of ionization than the one with which they are identified.

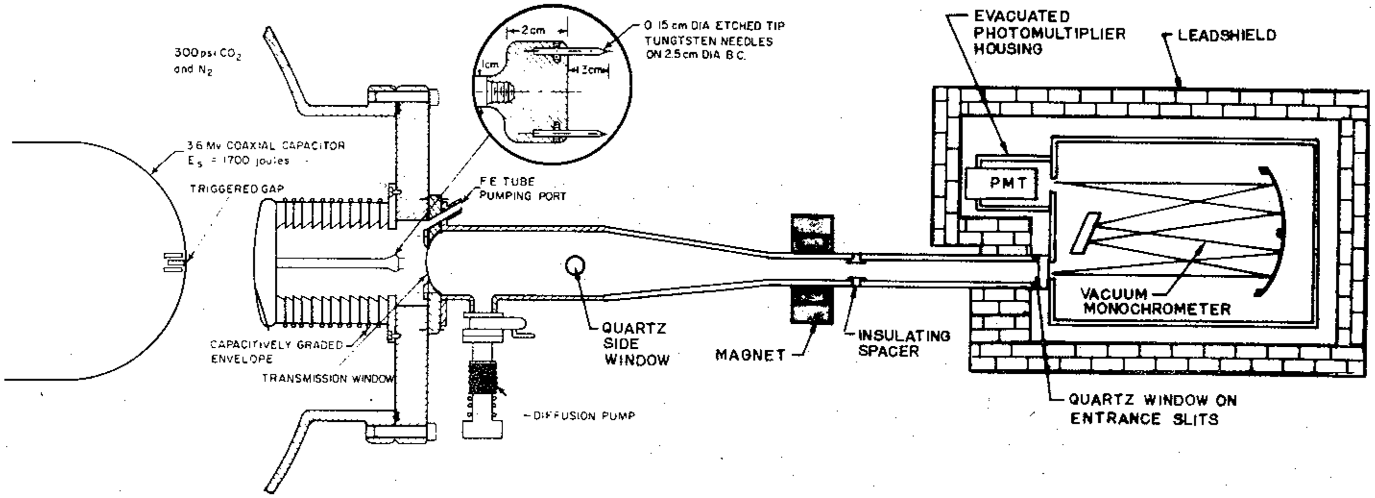

Figure 41. Vacuum UV Experimental Setup

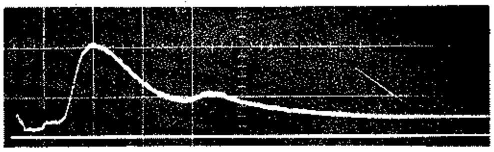

O^{I} 4368.30 Å Gain: 0.2 V/div Sweep: 10 μs/div

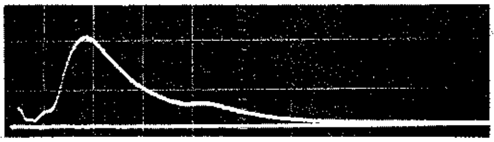

O^{II} 3008.4 Å Gain: 0.2 V/div Sweep: 10 μs/div

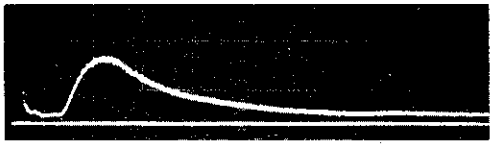

O^{III} 3759.82 Å Gain: 0.2 V/div Sweep: 5 μs/div

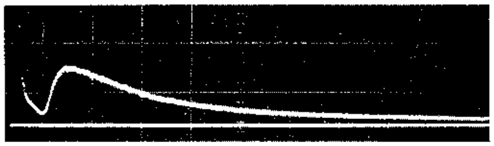

O^{IV} 3385.55 Å Gain: 0.2 V/div Sweep: 5 μs/div

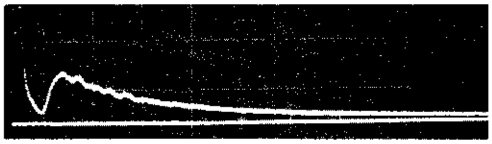

O^{V} 3144.68 Å Gain: 0.2 V/div Sweep: 5 μs/div

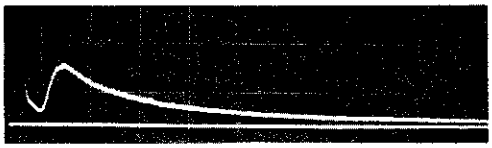

O^{VI} 3834.24 Å Gain: 0.2 V/div Sweep 5 μs/div

O^{VII} 2475.4 Å Gain: 0.2 V/div Sweep: 5 μs/div

Figure 42 Self-Stopped Electron Beam Produced Plasmas (Typical Oxygen Signatures)

2-945

The background is small compared to the intensities of the observed lines. There is a background noise trace which has a different signature than any of the lines. However, there are many more lines present than those identified and it is not clear whether the apparent variation in structure represents a real effect or misidentification due to the presence of unidentified lines. A sufficient number of transitions for statistical analysis, coupled with high resolution plate spectroscopy, would be required to clarify this point. (We do not have the instrumentation necessary to do such a survey.) The typical trace is presumed to be significant in this case. A series of nitrogen I through VI lines was also studied. They are not significantly different from the oxygen signatures.

4.5 Hydrogenic Lines

The last spectrum of any atom before complete ionization is hydrogenic. The spectral terms produced by the interaction of one electron and a bare nucleus are simpler and more easily calculated than spectra of more complicated ions. Thus, the computations of wavelengths, oscillator strengths and line broadening parameters are considered to be practical. Few of these transitions have been observed for most elements except in the X-ray region.

Predicted wavelengths of the hydrogenic transitions of O VIII and N VII were taken from a computation by Garcia and Mack(9) for the visible and near ultraviolet regions of the spectra. A survey was made of these predicted hydrogenic wavelengths to see whether they were excited by a self-focused electron beam. The experimental set-up of Figure 41 was used. In addition, the second (0.25 m) monochromator was focused on the tube center normal to the beam axis, through a quartz window, 44 cm from the beam entrance window and approximately 10 cm before the tapered section.

In general, spectral line emission has been observed at all the predicted wavelengths and tentatively identified as originating from transition of hydrogen like O VIII and N VII. These signatures show the same general shape as lower ionization level lines. Certain limited conclusions can be drawn from the gross features of these signatures. All lines in all levels of ionization when excited by a suitable self-compressed electron beam of $\nu/\gamma > 1/2$ show an emission for a few to hundreds of nanoseconds during and after the electron passage. This is followed by a dark period lasting microseconds and a recombinations emission lasting tens of microseconds or longer.

The length of the dark period reaches a maximum of drift tube pressures of 0.2 torr in oxygen and nitrogen and 1 torr in helium under all conditions so far observed. As all spectral line radiation ceases, the implication is that substantially all the atoms lying along the electron beam axis are fully stripped. At these pressures this implies that electron densities in the neighborhood of 5×10^{16} cm^{-3} are reached. This is only an indication, but it suggests that the densities are within the range of visible laser interferometry which is capable of absolute measurement.

The observed spectral line signatures, particularly of the hydrogenic series, are extremely sensitive to detailed parameters of the electron beam compression. An example of this sensitivity is shown in Figure 43. Axial view signatures are shown for the hydrogenic He II 3203 Å line for three different lengths of drift pipe, using the FX-1 accelerator. The length of the drift chamber has a clearly observable effect on the light emission and by implication on the formation of the plasma by the electron beam. It appears from previous arguments that a plasma of higher density is formed in the intermediate length chamber. If these signatures can be calibrated against absolute measurement, they will represent a sensitive, though complex indication of beam operating conditions.

A survey was also made of helium plasma. As helium has fewer lines than the other gases investigated, a photographic survey was made of the light emission parallel and perpendicular to the beam axis. The 0.25 m monochromator was adapted to photographic use and the spectra recorded on Polaroid film. From the photographs it was clearly noticeable that the higher series member of the visible series of lines of (hydrogenic) He II were much stronger relative to the other lines in the axial view than in the perpendicular view of

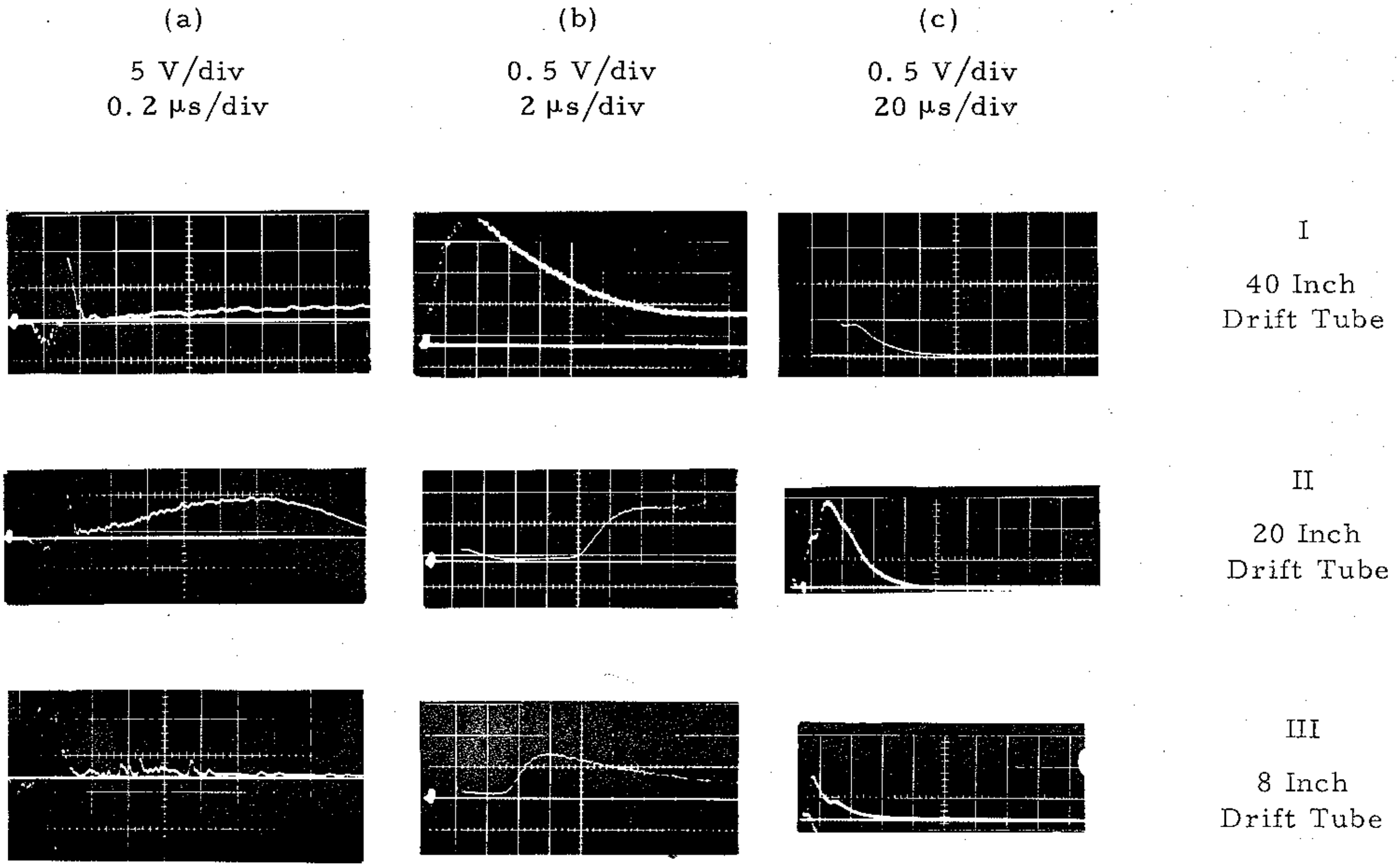

Figure 43 Axial $\mathrm{He^{II}}$ 3203 Å Line Signatures for Three Drift Tube Lengths

any previous observation of a helium discharge. As the axial view and normal view record different sections of the plasma, this implies only that the plasma is not uniform.

The 0.25 m monochromator was converted back to photoelectric readout. The HeIIβ 3203 Å line signature was observed through three ports, 5, 25 and 45 cm from the beam entrance window. The last window was 10 cm from the tapered section. Roughly the same signature was seen in all the ports but the amplitude of the signal in the second and third windows was two to three times that seen in the first one. After 100 μs there was still some light at the third port, less at the second, none at the first. Both observations are consistent with a plasma which changes with distance along the electron beam.

This adds another complication to the interpretation of the emission signatures. The spectral emission signatures depend on the details of the electron beam dynamics in both space and time. The axial view which sees a major part of the plasma gives a more uniform signature which remains substantially the same from pulse to pulse. The normal view is less stable and depends on the position of the instrumentation.

The two views show the same general signatures for at least some of the spectral lines. The gross features are identifiable in both, but the details vary. The size and shape of the early peaks, the length of the dark periods, the relative sizes of the emission peaks are often quite different in the two views. The two instruments are not of the same optical precision. The smaller monochromator which was used on the side view cannot be set to a wavelength as accurately, and has twice the wavelength acceptance for the same width slits as the larger instrument. It soon became apparent that the detailed signatures, at least for some O VIII lines depended on the wavelength settings. The lines were either very broad or were associated with other lines which were very broad.

4.6 Spectral Line Shapes

In addition to the basic line signatures which have been discussed, the hydrogenic lines and some of the lower level ion lines show anomalous features which are not explainable on the simple model so far discussed. The most obvious point is a second late emission peak which occurs at about 34 μs after the electron passage. This peak is maximized under the same conditions which maximize the length of the dark time before the recombination emission is seen.

In order to examine this effect, a spectral survey was performed using the FX-25 accelerator. Two spectral lines were chosen which showed the effect strongly O VIII 4340 Å and 2906 Å. Signatures were taken at 2 or 4 Å intervals across the spectral line on successive firings of the accelerator. Both axial and normal view signatures were observed using the two monochromators as before. Graphs were prepared from the signatures of the shape of the emitting lines at specific times in the discharge. Families of such emission spectra are shown in Figure 44 for the 4340 Å region axial view, in Figure 46 for the 4340 Å region normal view and in Figure 45 for the 2906 Å region axial view. The emission normal to the axis at the shorter wavelength was too small to be accurately measured.

From these graphs, it can be seen that there is a shift of the wavelengths of at least some of the spectral lines. In Figure 44 there appears to be a major unidentified spectral line which appears at 4359 Å. This line splits into two components which move apart and are separated by 20 Å by 0.8 μs having in the process overlapped the OVIII 4340 Å line which is clearly visible. All spectral light then ceases. After some 8 μs the components reappear and converge, finally rejoining after 34 μs. This last rejoined peak is large and broad enough to be seen as an anomalous peaks in adjacent spectral lines.

A similar effect is seen in Figure 45 for the 2906 Å region. In this case the line component spreading is observed but cannot be identified as originating from a single spectral line. In Figure 46, the view normal to the plasma in the 4340 Å region, shifting of the emission is seen, but no consistent spectral lines can be identified including the predicted OVIII 4340 Å transition.

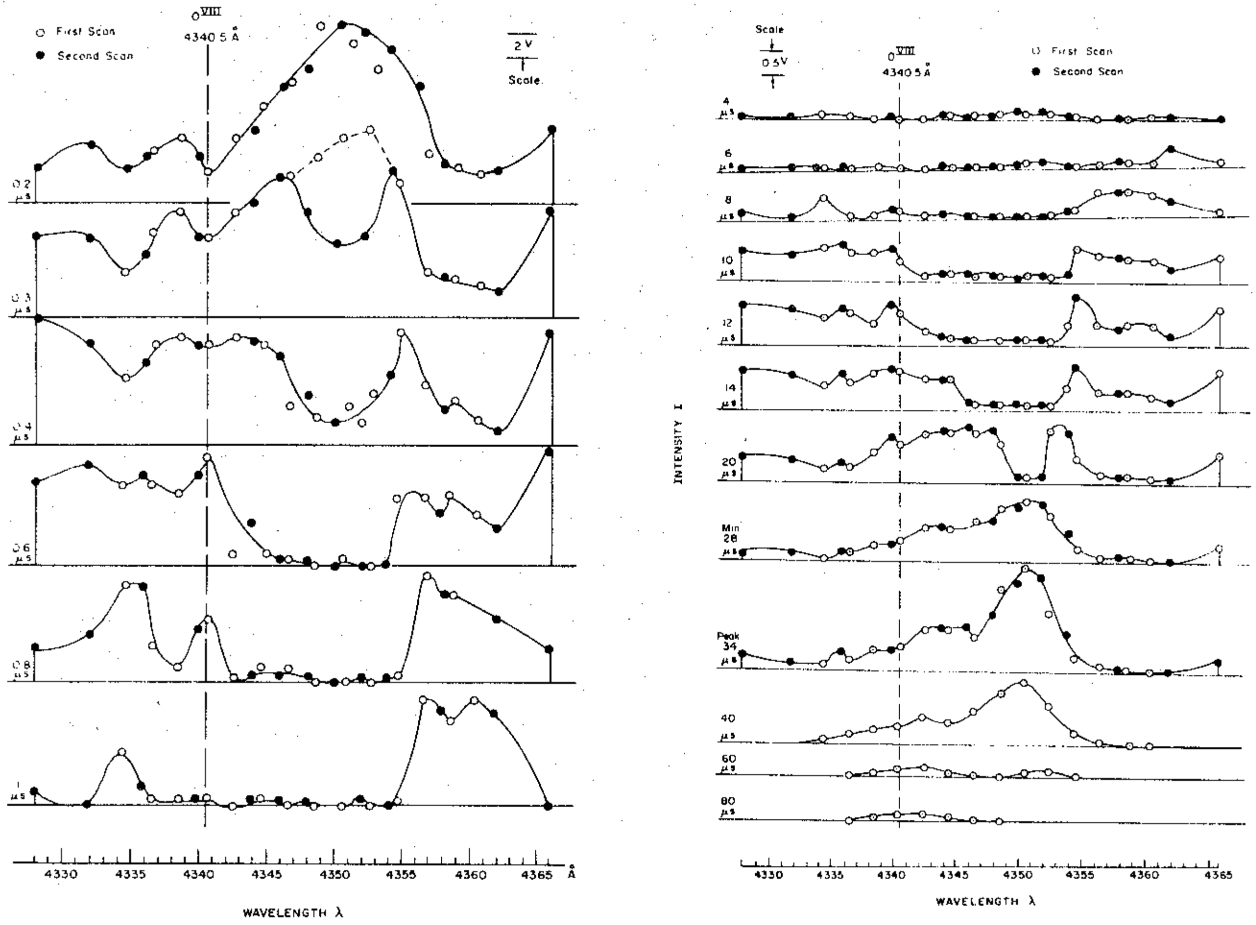

Figure 44. Oxygen Plasma Spectra (Axial View) Produced by Propagating $\nu/\gamma > 1/2$ Electron Beam Wavelength Region 4328 Å to 4366 Å

1-3593

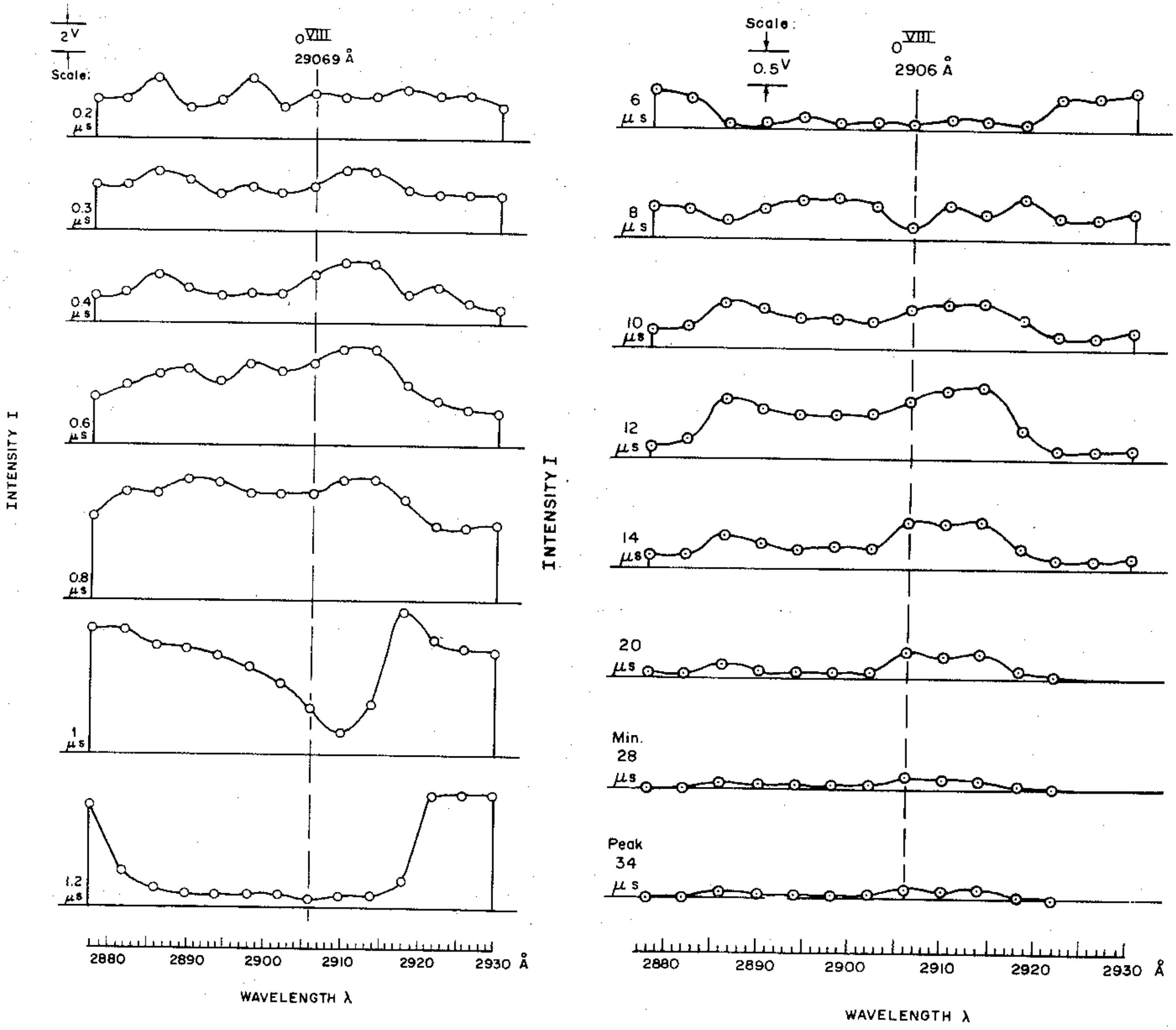

Figure 45. Oxygen Plasma Spectra (Axial View) Produced by Propagating $\nu/\gamma > 1/2$ Electron Beam Wavelength Region 2878 Å to 2930 Å

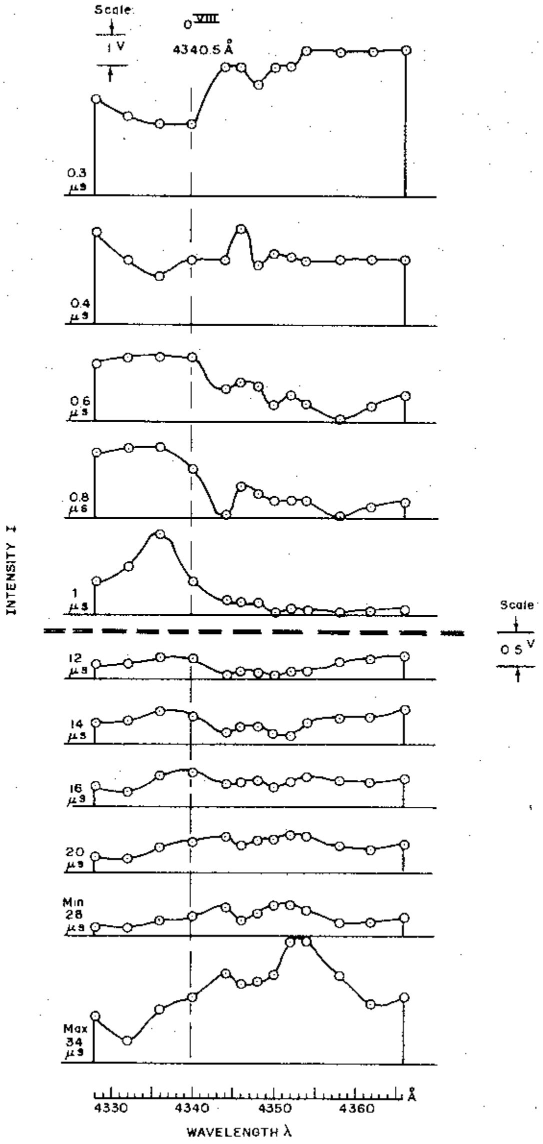

Figure 46. Oxygen Plasma Spectra (Normal View)
Produced by Propagating $\nu/\gamma > 1/2$
Electron Beam Wavelength Region 4328 Å to 4366 Å

Exactly what causes these line shifting effects is not clear. They appear as a function of the plasma collapse. Changes in the cathode or the drift tube configuration are reflected in the line signatures. This line broadening and shift did not appear in the plasma produced by a low ν/γ beam, such as was reported under the previous contract.(1) A number of physical mechanisms can produce line broadening and splitting. These include electron density, resonant trapping, magnetic fields and constant or radio frequency electric fields. It is not known what mechanism or combination of mechanisms causes the effects observed here. Too little data has been taken to be sure what the effect is or on what it depends. Both more experimental data and a theoretical analysis will be required in order to understand this observation.

4. 7 Summary

Spectroscopic diagnostic techniques were applied to propagating electron beams of $\nu/\gamma > 1/2$. It has been shown by cavity techniques that inverted populations occur in the resulting plasma and persist for a considerable time. Line signatures have been observed from all levels of ionization of oxygen and nitrogen. The signatures in all levels of ionization show a dark period after approximately 1 μs which is consistent with depletion of the levels by complete stripping of the atom. At the pressures used this implies that electron densities of 5×10^{16} cm^{-3} are reached. The hydrogenic series of lines of O VIII and N VII have been observed in those plasmas at the predicted wavelength. It is believed that the appearance of those transitions will prove particularly useful as their spectral characteristics can be calculated. Observation has been made of spectral lines which split into components which separate widely and converge late in time. Graphs of the behavior of these components have been obtained. The significance of these shifting components is not presently understood, but suggests the need for further investigation.

SECTION 5

THEORETICAL INVESTIGATIONS

5.1 Return Current in the Hydrodynamic Model

The problem of describing the induced volume currents generated by a relativistic electron beam penetrating a plasma is a very formidable undertaking. One is confronted with a system in which the plasma density, and temperature, is a unknown function of time. This means that the effective plasma conductivity is also a function of time, and the problem of solving Maxwell's equations with a time varying conductivity is too difficult to do analytically. To get some feeling for the time buildup of the induced return current, we will consider instead the case in which a beam is injected into a preformed plasma of constant conductivity. The beam is assumed uniform, and fills the whole volume of the drift tube.

Consider an electron beam of radius r_b penetrating a plasma of conductivity σ; we wish to find the induced return current using an exponential increase in the beam current as an approximation to the rapid increase in beam current as a pulse of electrons is injected into a bounded plasma.

The appropriate Maxwell's equations are:

$$\nabla \times \vec{E} = -\dot{\vec{B}} \tag{1}$$

$$\nabla \times \vec{B} = \mu_o \left[J_{beam} + J_{plasma} \right] \tag{2}$$

where J_{beam} and J_{plasma} are taken to be uniform in the z direction; in the hydrodynamic model the plasma conductivity is taken as constant (and displacement current is neglected in comparison to induced current in the plasma) so that:

$$J_{plasma} = \sigma E_z \tag{3}$$

From Equation (1):

$$\frac{\partial E_z}{\partial r} = \dot{B}_\theta \tag{4}$$

and from Equation (2):

$$\frac{1}{r}\frac{\partial}{\partial r}(r B_\theta) = \mu_o \left[J_{beam} + J_{plasma} \right] \tag{5}$$

Combining Equations (4) and (5), we get:

$$\frac{\partial}{\partial r}\left(r \frac{\partial E_z}{\partial r} \right) = \frac{\mu_o r}{\pi r_b^2} \dot{I}_{beam} + \mu_o r \sigma \dot{E}_z (r,t) \; r < r_b \tag{6}$$

where we have assumed a uniform beam, so that:

$$J_{beam} = \frac{I_{beam}}{\pi r_b^2}$$

Taking the Laplace transform of Equation (6), one obtains:

$$\frac{\partial}{\partial r}\left(r \frac{\partial E_z}{\partial r} (r,S) \right) = \left[S\, I(S) - I_o \right] \frac{r \mu_o}{\pi r_b^2} + \mu_o r \sigma S E_z (r,S) \tag{7}$$

or

$$\frac{\partial}{\partial r}\left(r\,\frac{\partial E_z}{\partial r}\right) - \mu_o\, r\, \sigma\, S\, E_z\,(r, S) = \left[S\, I\,(S) - I_o\right]\frac{r\,\mu_o}{\pi\, r_b^2}\quad r < r_b \tag{8}$$

The homogeneous solution to Equation (8) for the region inside the beam is:

$$\phi_n\,(r) \sim J_o\,(k_n\, r)\quad r < r_b$$

where the k_n's are defined by the requirement that the electric field be zero at the outer conductor (taken to be at the same radius as the beam):

$$\phi_n\,(r_b) = 0 = J_o\,(k_n\, r_b) \tag{9}$$

Then the general solution to Equation (8) is:

$$E_z = -\sum_n \frac{A_n\,(S)\, J_o\,(k_n\, r)}{\mu_o\,\sigma\, S + k_n^2} \tag{10}$$

where

$$A_n\,(S) = \left[\, S\, I\,(S) - I_o\right]\frac{\mu_o}{\pi\, r_b^2}\;\frac{\int_o^{r_b} r\, J_o\,(k_n r)\, dr}{\int_o^{r_b} r\, J_o^2\,(k_n r)\, dr}$$

$$= \left[S\, I(S) - I_o\right]\mu_o\, B_n$$

We want to examine the induced return current due to the return current due to the leading edge of the current pulse. For analytic simplicity, take the time dependence of the leading edge to be:

$$I = I_{max} \left[1 - e^{-\alpha t} \right] \tag{11}$$

where $\alpha \equiv 1/\tau$, and τ is the pulse risetime.

The front of the current pulse is thus modeled as shown in Figure 47. The transform of Equation (11) is then:

$$I(S) = I_{max} \left[\frac{1}{S} - \frac{1}{S + \alpha} \right] = I_{max} \left[\frac{\alpha}{S (S + \alpha)} \right] \tag{12}$$

Substitution of Equation (12) in Equation (10) yields:

$$E_z (r, S) = \frac{-1}{\mu_o \sigma} \sum_n B_n I_o (k_n r) \quad I_{max} \left[\frac{\alpha}{S + \alpha} \cdot \frac{1}{S + \beta_n} \right] \tag{13}$$

where:

$$\beta_n = \frac{k_n^2}{\mu_o \sigma}$$

and

$$B_n = \frac{1}{\pi r_b^2} \frac{\int_o^{r_b} r J_o (k_n r) \, dr}{\int_o^{r_b} r J_o^2 (k_n r) \, dr}$$

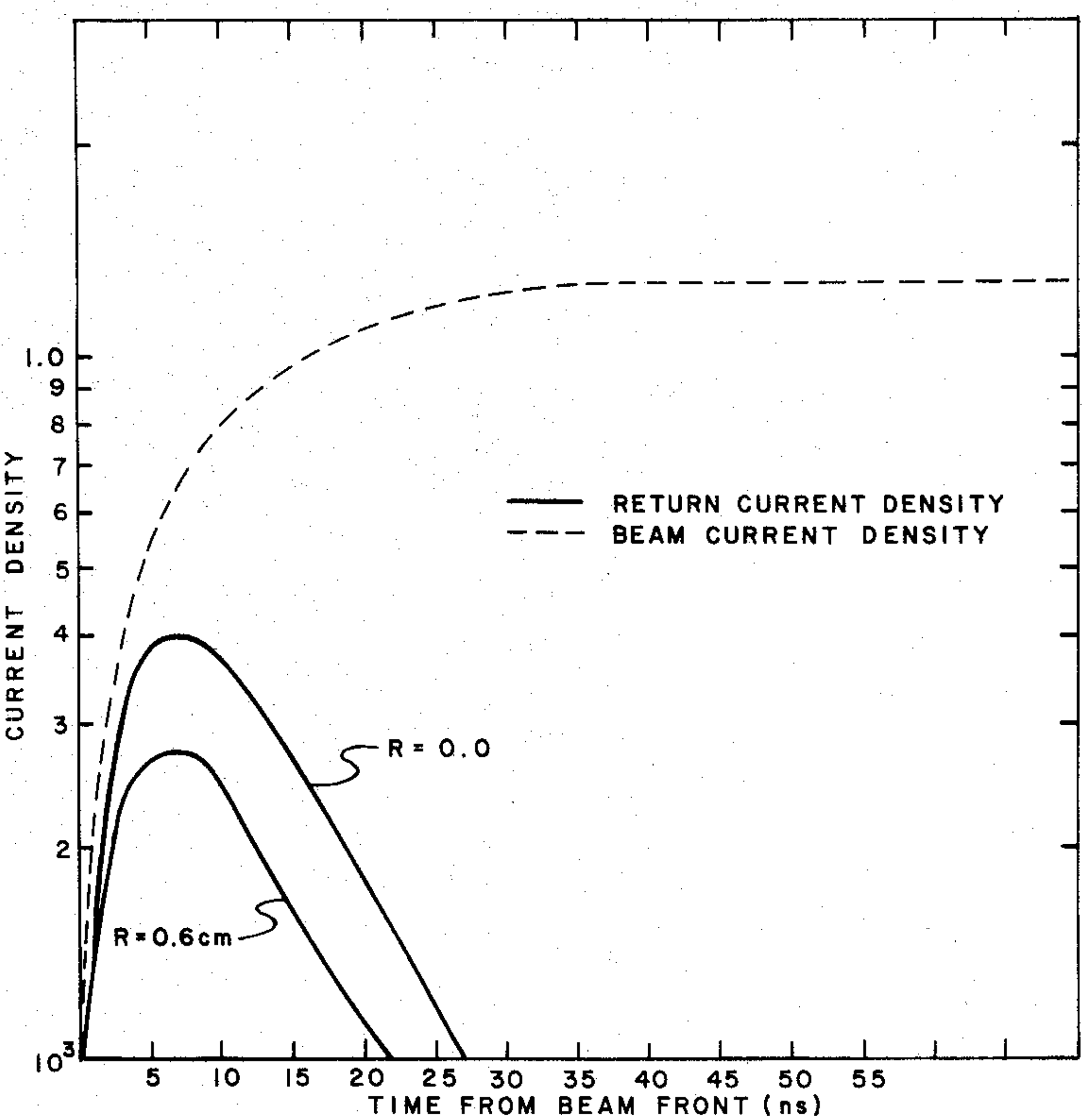

Figure 47. Return Current Density at Various Radii
σ = 2 mho/cm

1-3597

or

$$E_z\,(r, S) = -\frac{1}{\mu_o\,\sigma\,\tau} \sum_n B_n\,J_o\,(k_n\,r)\,I_{max} \left[\frac{\dfrac{1}{\beta_n - \alpha}}{S + \alpha} + \frac{\dfrac{1}{\alpha - \beta_n}}{S + \beta_n} \right] \tag{14}$$

Taking the inverse transform of Equation (14) yields the following:

$$E_z\,(r, t) = -\frac{1}{\sigma\,\tau} \sum_n \frac{B_n\,J_o\,(k_n\,r)}{\beta_n - \dfrac{1}{\tau}}\,I_{max} \left[e^{-t/\tau} - e^{-t\,\beta_n} \right]$$

or

$$E_z\,(r, t) = -\frac{I_{max}}{\sigma} \sum_n \frac{B_n\,J_o\,(k_n\,r)}{k_n^2\,\dfrac{\tau}{\mu_o\,\sigma} - 1} \left(e^{-t/\tau} - e^{-t\,k_n^2/\mu_o\,\sigma} \right) \tag{15}$$

The return current density will be given as:

$$J_z\,(r, t) = \sigma\,E_\gamma\,(r, t) = -I_{max} \sum_n \frac{B_n\,J_o\,(k_n\,r)}{k_n^2\,\dfrac{\tau}{\mu_o\,\sigma} - 1} \left(e^{-t/\tau} - e^{-t\,k_n^2/\mu_o\,\sigma} \right) \tag{16}$$

Before we can evaluate the return current, we must simplify the coefficients B_n; for the denominator, we can show the following; from the boundary conditions that $J_o\,(k_n\,r_b) = 0$:

$$\int_o^{r_b} r\,J_o^2\,(k_n\,r)\,d\,r = \frac{r_b^2}{2}\,J_1^2\,(k_n\,r_b)$$

also, from the properties of the Bessel function, we have for the numerator:

$$\int_0^{r_b} r J_o (k_n r) dr = \frac{r_b}{k_n} J_1 (k_n r_b)$$

Thus:

$$B_n = \frac{2}{\pi r_b^3 k_n J_1 (k_n r_b)}$$

Finally, substituting this value for B_n in Equation (16) obtains the following:

$$J_z (r, t) = \frac{-2 I_{max}}{\pi r_b^3} \sum_n \frac{1}{\left(\frac{k_n^2 \tau}{\mu_o \sigma} - 1\right) k_n} \frac{J_o (k_n r)}{J_o (k_n r_b)} x$$

$$(e^{-t/\tau} - e^{-t k_n^2/\mu_o \sigma})$$

(17)

5.2 Numerical Results

Some results obtained for the return current using Equation (17) are shown in Figures 47, 48 and 49. The parameters chosen for the calculations are as follows:

τ = risetime of beam = 10 ns

r_b = beam diameter = 1 cm

$$\sigma = \text{plasma conductivity} = \left\{\begin{matrix} 2 \\ 20 \\ 2 \times 10^4 \end{matrix}\right\} \text{ mho/cm}$$

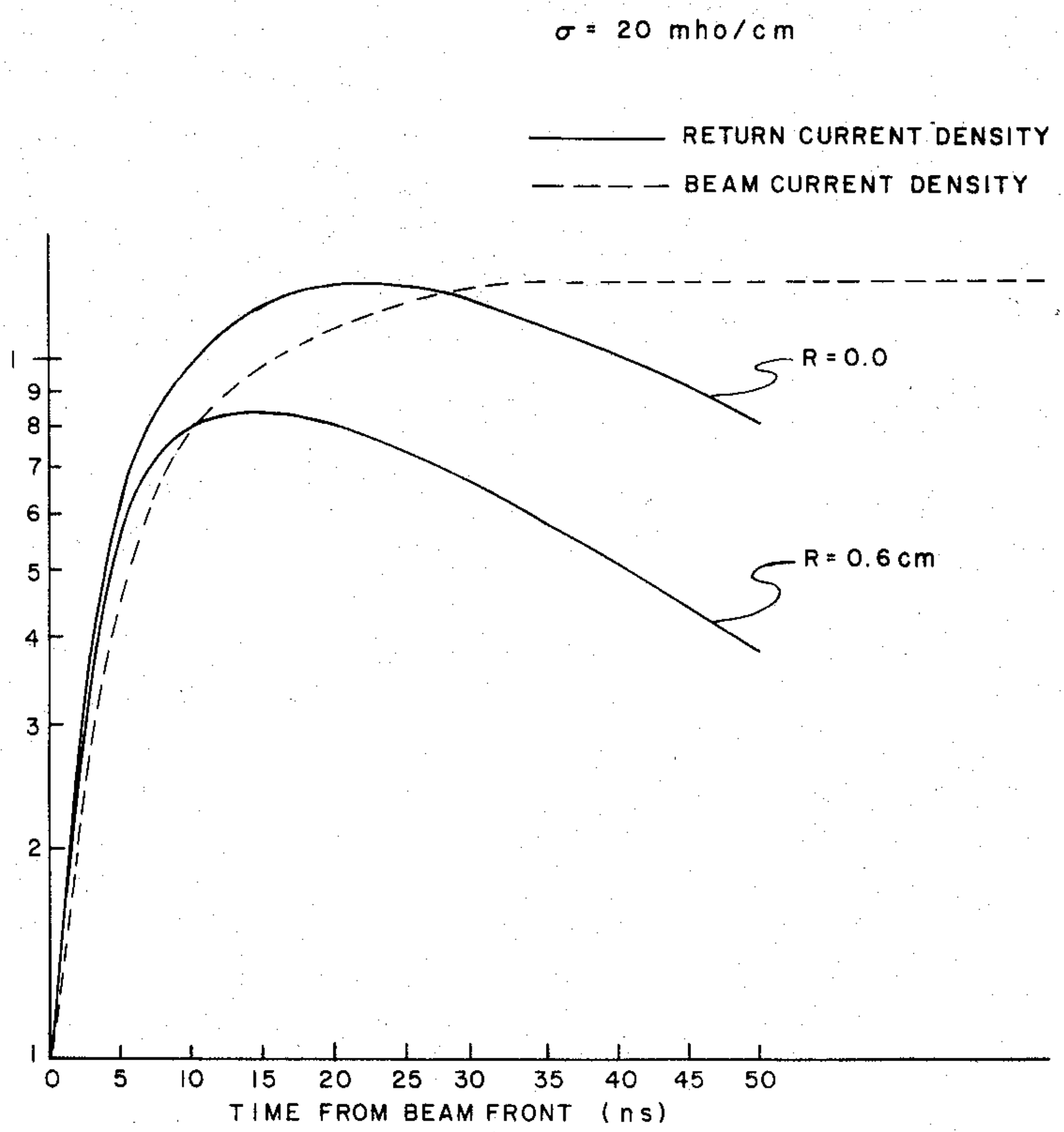

Figure 48. Return Current Density at Various Radii
$\sigma = 20$ mho/cm

1-3596

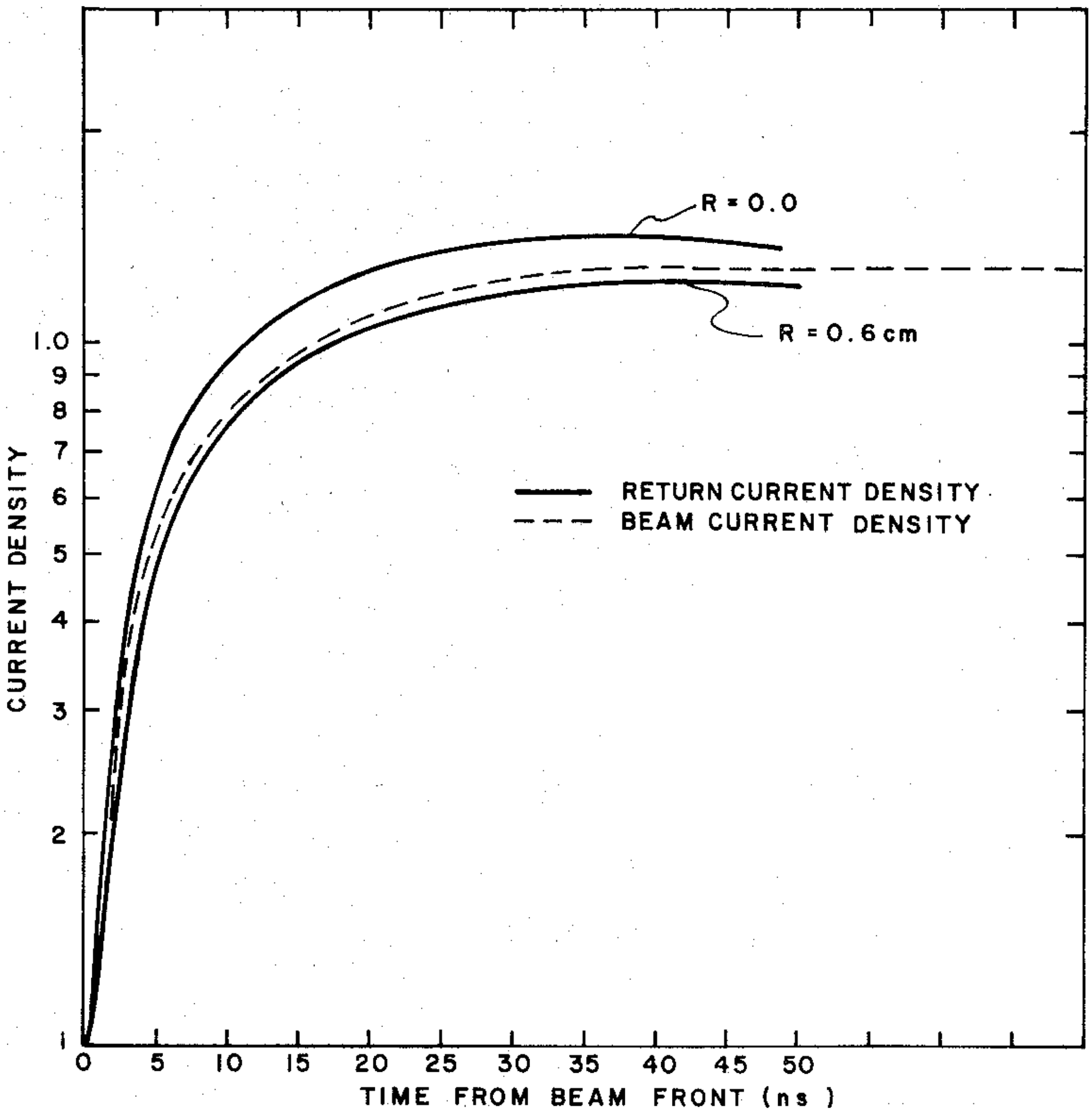

Figure 49. Return Current Density at Various Radii
$\sigma = 2.0 \times 10^4$ mho/cm

For low conductivity Figure 47 shows that the return current is low and lasts only as long as the beam is increasing and providing an induced back emf. For higher conductivity the return current density at the center of the beam is higher than the beam current density. The return current density holds up very much longer than the beam risetime, presumably because the induced back emf is dependent on the difference between the beam and return current. These features are shown in Figures 48 and 49.

5.3 Azimuthal Magnetic Field in the Wake of the Current Pulse

The beam formed plasma left in the wake of the intense current pulses has been observed to last for hundreds of nanoseconds. The confining mechanism for this late-time plasma must then be rather long time. The decay time for the wake magnetic field could be estimated from the diffusion time:

$$\tau = \mu_o \sigma L_D^2 \tag{18}$$

where σ is the conductivity of the plasma through which the magnetic field must diffuse and L is the diffusion length.

However, Yadavalli(11) has calculated the magnetic field in the wake of a pulse of current passing through a plasma in detail. In this section we discuss this calculation and some results obtained from a numerical computation using his formulation.

The hydrodynamic approach, wherein the plasma is represented by a real, constant conductivity, is employed. Figure 50 shows the configuration of the problem treated.

Maxwell's equations are written exactly as in the previous section for the electron beam penetrating the plasma, except displacement current is included. Yadavalli's calculation will, however, account for the finite length of the current pulse. Thus, we have:

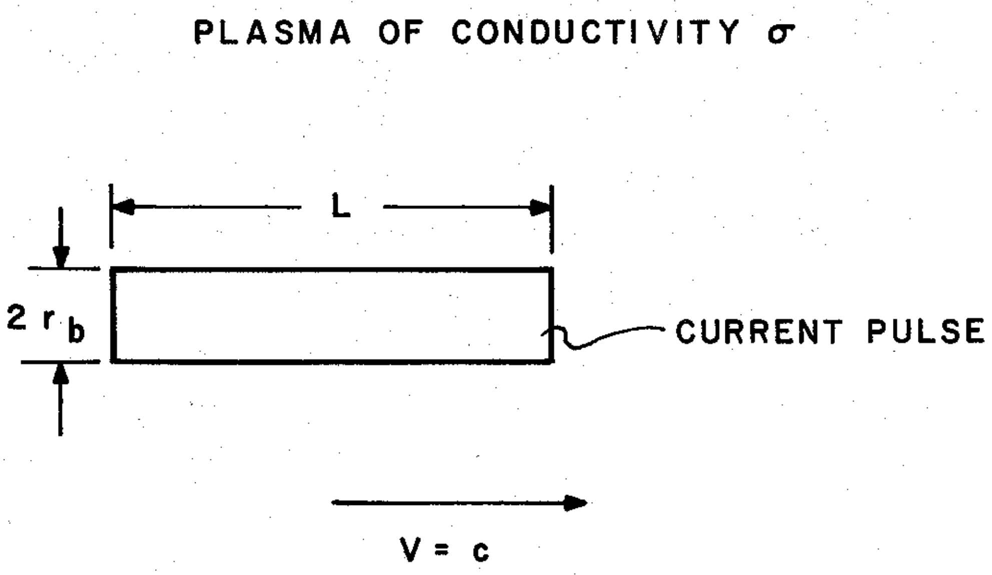

Figure 50. Model for Wake Calculation

$$\nabla \times \vec{E} = -\frac{\partial \vec{B}}{\partial t}$$

$$\nabla \cdot \vec{D} = q \tag{19}$$

$$\nabla \times \vec{H} = \vec{J}_{\text{beam}} + \vec{J}_{\text{plasma}} + \frac{\partial \vec{D}}{\partial t}$$

From Equation (19), we form the wave equation:

$$-c^2 (\vec{\nabla} \times \vec{\nabla} \times \vec{E}) = \frac{1}{\epsilon_o} \left(\sigma \frac{\partial \vec{E}}{\partial t} + \vec{v} \frac{\partial q}{\partial t}\right) + \frac{\partial^2 \vec{E}^2}{\partial t^2} \tag{20}$$

Fourier transforming Equation (20) one obtains the following for $\vec{B}$ in the k domain (k is the wave number):

$$\vec{B}(k) = \frac{\left(\frac{i}{\epsilon_o}\right)(\vec{k} \times \vec{v})\, q(k)}{k^2 c^2 - (\vec{k} \cdot \vec{v})^2 - \frac{i}{\epsilon_o}(\vec{k} \cdot \vec{v})\,\sigma} \tag{21}$$

q is the charge density in the current pulse; in the frame of the pulse it is written:

$$q(\vec{r}) = q_{\perp}(r)\, q_{\parallel}(z) \tag{22}$$

The charge density is taken as uniform in the z direction:

$$\begin{aligned} q_{\parallel}(z) &= \text{constant} \quad -L < z < 0 \\ &= 0 \quad\quad\quad\;\; \text{otherwise} \end{aligned}$$

In the r direction, the beam profile for the model considered is:

$$q_{\perp}(r) = \left(1 - \frac{r^2}{r_b^2}\right) \qquad r < r_b \tag{23}$$

$q_{\perp}(r)$ and $q_{\parallel}(z)$ are Fourier transformed separately and substituted into Equation (21). After performing the inverse transformation and integrating, Yadavalli finally obtains the following for $B_\theta(r_b, z)$ in the wake:

$$B_\theta(r_b, z) = \frac{\mu_o I}{4 r_b} \left[\zeta_- \; {}_3F_3\left(2, \frac{5}{2}, 1; 3, 2, 4; -2\zeta_-\right) - \zeta_+ \; {}_3F_3\left(2, \frac{5}{2}, 1; 3, 2, 4; -2\zeta_+\right) \right] \tag{24}$$

where:

$$\zeta_- = \frac{r_b^2 \sigma}{\epsilon_o c} \frac{1}{z} = r_b^2 \frac{Z_o \sigma}{z}$$

Z_o = impedance of free space

$$\zeta_+ = r_b^2 \frac{Z_o \sigma}{(z + L)}$$

and ${}_3F_3$ is the generalized hypergeometric function defined as follows:

$$_3F_3(\alpha_1, \alpha_2, \alpha_3; \beta_1, \beta_2, \beta_3; y) = \sum_{n=0}^{\infty} \frac{(\alpha_1)_n (\alpha_2)_n (\alpha_3)_n \, y^n}{n! \, (\beta_1)_n (\beta_2)_n (\beta_3)_n}$$

$$(\alpha)_n = \alpha(\alpha + 1)(\alpha + 2) \ldots (\alpha + n - 1) \qquad (25)$$

$$(\alpha)_o = 1$$

$$(\beta)_n = \beta(\beta + 1)(\beta + 2) \ldots (\beta + n - 1)$$

$$(\beta)_o = 1$$

The results of the computer calculations are summarized in Figure 51, where the decay time rather than decay distance, has been plotted against conductivity. The decay time increases for values of conductivity up to about 4.5×10^2 mho/cm. This behavior is what one would expect for frozen in magnetic fields. For low values of conductivity, the decay time as predicted by Equation (18) for $\sigma = 80$ mho/cm and $L_D = R_b = 0.5$ cm is:

$$\tau = \mu_o \sigma R_b^2 \cong 250 \text{ ns}$$

The decay time for the same conductivity as predicted by Equation (24) is, from Figure 51:

$$\tau = 216 \text{ ns}$$

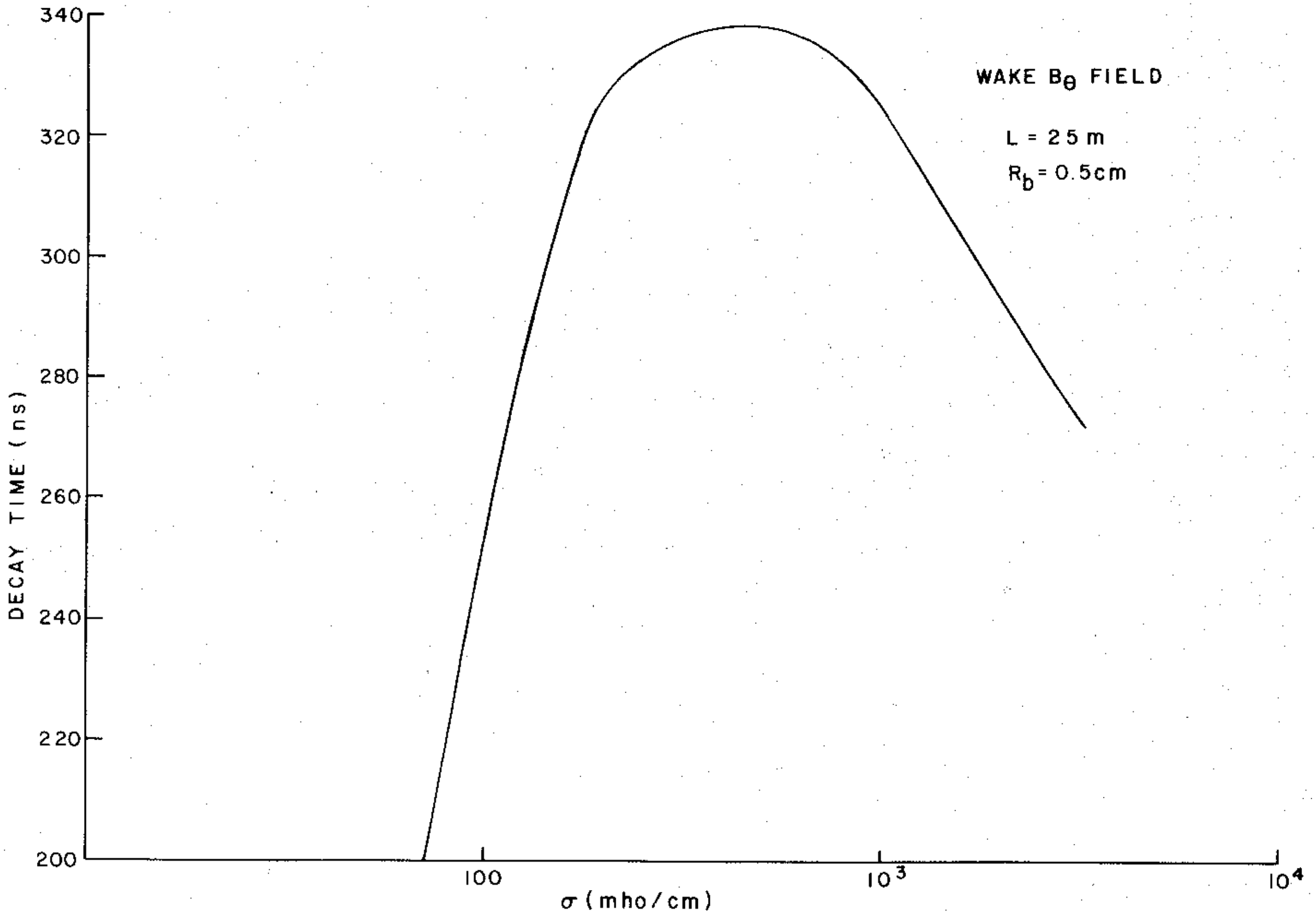

Figure 51. Wake Magnetic Field Intensity

However, for higher values of conductivity, the magnetic field in the wake does not last as long as a simple diffusion model would indicate, and in fact the decay time falls off with higher values of conductivity. This is probably due to induced return currents which prevent the azimuthal magnetic field from ever being formed in the first place.

Unfortunately, we cannot readily investigate the early time behavior of the wake magnetic field for high values of conductivity, because of the aforementioned convergence problem.

SECTION 6

REFERENCES

(1) Final Report, Contract DA-49-146-XZ-553, 1968

(2) Interim and Final Report, Contract DA-01-68-C-0051

(3) G. Lehner and F. Pohl, "Neutrons from d-d Reactions as a Tool for Plasma Diagnostics", Report IPP 1/60, March 1967, Institute for Plasma Physics, Garching, Germany

(4) The neutron yield data are from a compilation of data by E. A. Burrill of High Voltage Engineering Corporation in an intermal document entitled "Neutron Production and Protection"

(5) S. E. Graybill and S. V. Nablo, Appl. Phys. Letters, 8, 18 (1966)

(6) S. E. Graybill, J. Uglum and S. V. Nablo, Bull APS, 11, 56 (1968

(7) V. I. Veksler, Atomnaya Energiya, 2, 247 (1957)

(8) P. K. Cheo and H. G. Cooper, J. Appl. Phys., 36, 1862 (1965)

(9) W. L. Wiese, M. W. Smith and B. M. G. Lennon, "Atomic Transition Probabilities", Volume I, NSRDS-NBS-4, National Standard Reference Data Series, National Bureau of Standards Washington, D. C. (1966)

(10) J. D. Garcia and J. E. Mack, Journal of the Optical Society of America, 6, 654 (1965)

(11) S. V. Yadavalli, "Electromagnetic Wake of a Charged Particle Pulse in a Plasma", The Physics of Fluids, Volume 8, p. 956 May 1965

PUBLICATIONS RESULTING FROM THIS CONTRACT

"Spectroscopic Observations of Self-Compressed Electron Beam Produced Plasmas", J. Rizzo, to be presented at APS Washington Meeting, 1969.

"Spectroscopic Observations of Self-Compressed Electron Beam Produced Plasmas", J. Rizzo, Ion Physics Technical Report 808-TR-338, submitted to Journal of Applied Physics.

"Observation of Energetic Ion Flow from a Beam Generated Plasma", J. Uglum, S. Graybill, Ion Physics Technical Report to be published.

"Dynamics of Electron Beam Flow from Pulsed, High Current 'Field Emission' Cathodes", W. H. McNeill and J. R. Uglum, IEEE Nuclear Science Transactions, Proceedings of 1969 National Accelerator Conference (1969).

"Beam Characteristics of Intense Relativistic Electron Beam Accelerators", J. Uglum, W. McNeill, S. Graybill, Proceedings of 10th Symposium on Electron, Ion, and Laser Beam Technology (1969).

"Pulsed Field Emission Cathode Emittance Measurements", J. R. Uglum, S. E. Graybill, S. V. Nablo, to be published in Reviews of Scientific Instruments (1969).

"Electron Beam Stopping due to Self-Magnetic Compression", S. Graybill, J. Uglum, S. Nablo, Bull. APS, 13, 56 (1968).